Characterization and modulation of human insulin degrading enzyme conformational dynamics to control enzyme activity

Jordan M. Mancl[1], Wenguang G. Liang[1,5], Nicholas L. Bayhi[2], Hui Wei[3,6], William Budell[3], Joshua H. Mendez[3], Tobin R. Sosnick[4], Bridget Carragher[3,7], Clinton S. Potter[3,7] and Wei-Jen Tang[1]*

1. Ben-May Institute for Cancer Research, The University of Chicago, 929 East 57th Street, Chicago, Illinois 60637, USA

2. Graduate Program in Biophysical Science, The University of Chicago, 929 East 57th street, Chicago, Illinois 60637, USA

3. Simons Electron Microscopy Center, New York Structural Biology Center, 89 Convent Ave, New York, New York, 10027, USA

4. Department of Biochemistry and Molecular Biology, The University of Chicago

5. Current affiliation - Bayer HealthCare Pharmaceuticals LLC, St Louis, Missouri, USA

6. Current affiliation - Rutgers New Jersey Medical School, Newark, New Jersey, USA

7. Current affiliation - Chan Zuckerberg Institute for Advanced Biological Imaging, Redwood City, California, USA

* Corresponding author

Email: wtang@uchicago.edu

Author Contributions: W.-J.T., J.M.M., W.G.L. designed the project. For the molar ratio of IDE to insulin of 2 to 1 cryo-EM analysis, W.G.L. performed protein purification, cryo-EM grid preparation, data acquisition and processing assisted by H.W. and overseen by W.-J.T., B.C. and C.S.P. J.M.M. and W.G.L. built and refined structural models. J.M.M. performed heterogeneity analysis of cryo-EM structures, MD simulations, and mutant characterizations. For time-resolved CryoEM analysis, J.M.M. performed protein purification, W.B. performed cryo-EM grid preparation, J.H.M performed data acquisition, and J.M.M. performed data processing and model building. N.L.B performed the Upside simulations and analysis and initial all-atom MD simulations under the guidance of T.R.S. J.M.M. W.-J. T. wrote the manuscript and all authors contributed to manuscript finalization.

Acknowledgement: We would like to thank our colleagues at the University of Chicago: Adam Antoszewski and Aaron Dinner for providing us with the data from their insulin unfolding simulations, as well as Rong Shen for general guidance with the MD simulations, and Jessica Martinez Martinez for assistance with cloning the IDE R668A construct. We would also like to thank James Byrnes at the LiX beamline at Brookhaven National Laboratory for collecting SEC-SAXS data. Computer resources came, in part, from an allocation on the Beagle3 computing cluster at the University of Chicago. This work was supported by the NIH grant GM121964 to W.-J. Tang. The Simons Electron Microscopy Center is supported by a grant from the Simons Foundation (SF349247). Use of the Advanced Photon Source was supported by the U.S. Department of Energy, Office of Basic Energy Sciences, under contract No. DE-AC02-06CH11357. The

LiX beamline is supported by NIH grants P30GM133893 & S10 OD012331, DOE grants KP1605010 & DE-SC0012704.

Competing Interest Statement: None.

Keywords (5 max): amyloid peptides, insulin degrading enzyme, proteostasis, diabetes, cryo-electron microscopy

Abstract

Insulin degrading enzyme (IDE) is a dimeric M16A zinc metalloprotease that degrades amyloidogenic peptides diverse in shape and sequence, including insulin and amyloid-β, to prevent toxic amyloid fibril formation. IDE has a hollow catalytic chamber formed by two ~55 kDa N- and C- domains (IDE-N and IDE-C, respectively), in which peptides bind, unfold, and are repositioned for proteolysis. IDE is known to transition between a closed state, poised for catalysis, and an open state, able to release cleavage products and bind new substrate. Here, we present five cryo-EM structures of the IDE dimer at 3.0-4.1 Å resolution, obtained in the presence of a sub-saturating concentration of insulin. Combining cryo-EM heterogeneity analysis with all-atom molecular dynamics (MD) simulations, we identified the structural basis and key residues for IDE conformational dynamics that were not revealed by IDE static structures. Notably R668 serves as a molecular latch mediating the open-close transition and facilitates key protein motions through charge-swapping interactions at the IDE-N/C interface. Our small-angle X-ray scattering and enzymatic assays of an R668A mutant indicate a profound alteration of conformational dynamics and catalytic activity. By integrating coarse-grained Upside MD simulations, our analysis reveals that IDE unfolds its substrates through the coordinated motion between IDE-N and IDE-C, as well as β-sheet formation between IDE and insulin. Additionally, our time-resolved cryo-EM analysis uncovers IDE allostery within the IDE dimer. Collectively, our findings demonstrate the strength of combining experimental and computational approaches to probe protein dynamics and pave the way for developing substrate-specific modulators of IDE activity.

Introduction

Protein homeostasis (a.k.a. proteostasis) is maintained by three primary mechanisms: chaperones, ubiquitination/proteasome, and autophagy (Hipp *et al*, 2019; Lopez-Otin *et al*, 2013). Disruptions in proteostasis can lead to the accumulation of amyloid fibrils and subsequent human diseases (Chiti & Dobson, 2006; Chiti & Dobson, 2017; Greenwald & Riek, 2010). As a result, many proteases have evolved to specifically target amyloidogenic peptides (Malito *et al*, 2008; Saido & Leissring, 2012). Among those, the cryptidase family, which includes the M16 metalloproteases insulin degrading enzyme (IDE) use an internal catalytic chamber, or "crypt", to capture and selectively degrade the monomeric form of amyloid peptides to control the formation of amyloid fibrils (Liang *et al*, 2022; Malito *et al.*, 2008). IDE effectively degrades various bioactive peptides, including amyloid-β (Aβ), a peptide associated with the progress of Alzheimer's disease, and three blood glucose-regulating hormones: insulin, amylin, and glucagon (Tang, 2016). Consequently, defects in IDE alter the progression of type 2 diabetes mellitus and Alzheimer's disease in animal models and are linked to these diseases in humans (Bertram *et al*, 2000; Bertram *et al*, 2007; Farris *et al*, 2003; Farris *et al*, 2004; Kim *et al*, 2007; Sladek *et al*, 2007; Tang, 2016; Tanzi & Bertram, 2005; Zeggini *et al*, 2007). IDE is a promising therapeutic target, as its inhibition improves glucose tolerance, yet progress has been hampered by the contrary actions of its diverse substrate pool (Maianti *et al*, 2014; Maianti *et al*, 2019; Tang, 2016). For example, IDE overexpression has been shown to reduce Aβ loads, in mice, however, this reduction is accompanied by hyperglycemia from a similar reduction in insulin levels (Leissring *et al*, 2003).

IDE-mediated substrate recognition and degradation is a complex process. IDE is capable of degrading substrates with diverse sequences and structures, such as Aβ and the three glucose-regulating hormones: insulin, amylin, and glucagon (Malito *et al.*, 2008; Tang, 2016). Despite this diversity, IDE exhibits high selectivity—for example, it preferentially degrades insulin and atrial natriuretic peptide over insulin-like growth factor-1 and brain natriuretic peptide, respectively (Malito *et al.*, 2008). The presence of ATP, inositol phosphate, or specific mutations can markedly enhance the catalytic rate for small peptide substrates like bradykinin, but does not significantly affect the degradation of larger substrates such as insulin and Aβ (Im *et al*, 2007; McCord *et al*, 2013; Song *et al*, 2017; Song *et al*, 2004). Additionally, the binding location of IDE inhibitors within the catalytic chamber can influence substrate preference, making IDE more likely to degrade one substrate over another (Charton *et al*, 2014; Maianti *et al.*, 2019). This complexity arises partly from the interplay between IDE's unfoldase and protease activities, which are essential for degrading diverse substrates (Malito *et al.*, 2008; Tang, 2016; Zhang *et al*, 2018). IDE relies on its unique large catalytic chamber and associated conformational dynamics to unfold and degrade amyloidogenic substrates. A deeper understanding of the molecular mechanisms by which IDE utilizes its catalytic chamber for substrate unfolding and degradation is crucial for effectively harnessing this enzyme in future therapeutic development.

IDE is a dimeric 110 kDa metalloprotease. Each protomer is comprised of four homologous subdomains organized into two ~55 kDa domains, IDE-N and IDE-C, connected by a short flexible linker

97 (Li *et al*, 2006; Shen *et al*, 2006) (Fig. 1A). Our previous cryo-EM analysis revealed the major conformational
98 states of IDE. In the absence of substrate, each protomer was found to adopt an open (O) or partial open
99 (pO) state which are primarily differentiated by the displacement of IDE-N relative to IDE-C, the combination
100 of which led to three dimeric conformations (O/O, O/pO, pO/pO) (Zhang *et al.*, 2018). It was observed that
101 substrate binding induced both protomers of IDE to fully close, referred to as the partial closed (pC, pC/pC
102 for the dimer) state, as the cryo-EM closed state was found to be slightly more open than previously solved
103 crystal structures, likely influenced by the constraints of the crystal lattice (McCord *et al.*, 2013; Shen *et al.*,
104 2006). Only the O state permits substrate access to the catalytic chamber, yet the catalytic cleft is stabilized
105 only in the pC state with substrate bound, requiring IDE to undergo a substantial open-close transition
106 during catalysis, the specifics of which are unknown (Zhang *et al.*, 2018).

107 Biochemical and structural analyses indicate that many IDE substrates, such as insulin, must first
108 be unfolded prior to cleavage (Fig. 1B, C). The conformational dynamics of IDE are thought to play a central
109 role in substrate recognition and degradation, yet several mechanistic details underlying IDE's unfoldase
110 activity remain unresolved (Fig. 1). We hypothesize that the unfoldase and protease activities of IDE are
111 regulated by the relative motions of the IDE-N and IDE-C domains, their interactions with substrates, and
112 allosteric communication between subunits within the IDE dimer. To investigate this, we solved cryo-EM
113 structures of IDE bound to insulin at a 2:1 IDE:insulin ratio, as well as structures captured following rapid
114 mixing of IDE with insulin under functionally relevant conditions. Utilizing newly developed computational
115 methods, we analyzed particle heterogeneity in these structures to infer IDE's conformational dynamics. By
116 integrating these experimental data with all-atom and coarse-grained molecular dynamics (MD)
117 simulations, we identified and modulated specific molecular interactions to manipulate IDE's key
118 conformational dynamics, ultimately enhancing our understanding how to control its enzymatic activity in
119 vitro.

120 **Results**

121 **Cryo-EM reveals new IDE structures in the presence of a sub-saturating concentration of insulin**

122 We have previously used cryo-EM to solve the structure of IDE in the presence of a 5-fold molar
123 excess of insulin, resulting in a dominant pC/pC state with both substrate binding chambers yielding density
124 corresponding to unfolded insulin (Zhang *et al.*, 2018). To explore the mechanism of IDE-directed substrate
125 unfolding under more physiologically relevant conditions, here we investigated IDE-insulin interactions with
126 an IDE:insulin molar ratio of 2:1. We collected a dataset of ~7,600 micrographs on a Titan Krios operated
127 at 300 keV, from which 7.2 million particles were picked for processing in RELION. Following an established
128 workflow, and processing the data with C1 symmetry, we generated 5 structures: three previously observed
129 structures with improved resolution (pC/pC, O/O, and O/pO at 3.0 Å, 3.8 Å, and 4.1 Å resolution) and two
130 novel states (O/pC and pO/pC at 3.4 Å and 3.3 Å resolution, respectively) (Fig. 2A, Figure 2 – figure
131 supplement 1, Supplementary file 1). Interestingly, the pC/pC was still found to be dominant, despite IDE

132 and insulin being present at a 2:1 molar ratio, consistent with the allostery of IDE (McCord *et al.*, 2013;
133 Zhang *et al.*, 2018).

134 The individual protomers of IDE adopt the same three conformations: O, pO, and pC states,
135 reported previously but there are significant differences in the O and pO states (Fig. 2B) (Zhang *et al.*,
136 2018). While the pC/pC state is nearly identical to the two states reported previously (RMSD of ~0.6 Å; PDB
137 ID: 6BFC, 6B3Q) (Zhang *et al.*, 2018), the O and pO states appear more closed when insulin is present,
138 suggesting that the presence of insulin promotes the open to closed transition. Specifically, the pO and O
139 subunits are 3-5 Å more closed based on the distance between the centers-of-mass (COM) of the IDE D1
140 and D4 subdomains, while the dihedral angle formed by the COM of the D1-D2-D3-D4 subdomains is
141 reduced by 5-10° (Fig. 2B). Alignment of the new O/O and O/pO states to their previously solved
142 counterparts reveals little difference, with a global RMSD of 1.316 Å (O/O, PDB ID: 6B7Y) and 1.405 Å
143 (O/pO, PDB ID: 6BF8), respectively (Zhang *et al.*, 2018). The primary source of variation between the
144 different states remains the degree of opening between the two domains of each subunit, as a global
145 alignment of IDE-N and IDE-C across all structures reveal the domains primarily act as rigid bodies (RMSD
146 <1.4 Å). Consistent with previous observations, the door region, which contains the catalytic zinc binding
147 site, exhibited higher B-factors in the O states than in either the pO or pC state (Zhang *et al.*, 2018) (Figure
148 2 – figure supplement 2).

149 All five cryo-EM structures presented here contain four subunits that have clear density present at
150 the catalytic cleft and exosite indicative of bound substrate, thus adopting the pC state. Previous structures
151 have modeled the same chain of insulin in both the exosite and catalytic cleft, but the best models we could
152 build into our density suggest that the chain bound to the exosite is not the same chain positioned for
153 cleavage at the catalytic cleft (Fig. 2C). The preponderance of data suggests it to be unlikely that insulin
154 adopts a preferred orientation within the catalytic chamber, rather the catalytic chamber can accommodate
155 insulin in four different orientations, with either the A or B chain bound to the exosite and catalytic cleft in
156 *cis* and *trans* orientations. This promiscuity of binding has been theorized as a reason for why there is no
157 chain preference for the initial insulin cleavage event (Manolopoulou *et al*, 2009). Crystal structures of
158 insulin are highly compact and globular, with little spatial separation between the N- and C- termini of each
159 chain, and the IDE cleavage sites are located within α-helices (Baker *et al*, 1988). In its crystallized state,
160 insulin cannot interact with both the exosite and catalytic cleft unless it unfolds, at least partially. Recent
161 work used MD simulations to study the conformational dynamics of insulin in solution and identified several
162 major "elements of disorder" to describe the partially unfolded intermediate structures they observed (Busto-
163 Moner *et al*, 2021). We docked these structures of insulin into the closed catalytic chamber of IDE and
164 found that the chamber was able to easily accommodate the positioning of either chain near the exosite
165 and catalytic cleft in *cis* and *trans* orientations (Figure 2 – figure supplement 3).

166 **Heterogeneity analysis reveals 2 dominant components of structural variability with the IDE cryo-**
167 **EM particle population**

168 Numerous structures of IDE exist with subunits adopting either an open or closed conformation,
169 yet we lack an understanding of how IDE transitions from an open to a closed state. The simplest
170 explanation of this transition, based on structural data, would be a direct, rigid body translation of IDE-N
171 relative to IDE-C, and this is the predominant model within the field (Shen *et al.*, 2006; Zhang *et al.*, 2018).
172 To better understand what this transition would look like, we measured and plotted the changes in the D1-
173 D4 COM distance versus the changes in the D1-D2-D3-D4 COM dihedral angle for all available cryo-EM
174 structures of IDE (Figure 3 – figure supplement 1). We found that in the absence of substrate, the transition
175 pathway produced a linear relationship between states. However, when our structures generated in the
176 presence of insulin were analyzed, the linear relationship no longer held (Figure 3 – figure supplement 1),
177 suggesting that the simple linear transition typically presumed for the open-close transition between distinct
178 IDE states does not accurately depict the complexity of IDE dynamics.

179 Recently, several approaches have been developed to understand the conformational
180 heterogeneity present within cryo-EM data. We employed multibody analysis in RELION and 3D variability
181 analysis (3DVA) in cryoSPARC to investigate the conformational heterogeneity within our particle
182 populations (Nakane *et al*, 2018; Punjani & Fleet, 2021). Of these, the range of motion predicted by
183 multibody analysis most closely matched the reported structures while 3DVA exhibited consistent results
184 across a smaller magnitude of transition (Figure 3 – figure supplements 1-3). Therefore, we focused on
185 multibody analysis below. Multibody analysis models the structural heterogeneity in our data as the result
186 of motions of independent, user-defined rigid bodies. As discussed above, the primary source of structural
187 variation in our structures is the positioning of IDE-N relative to IDE-C. We see little structural changes
188 within the domains, suggesting that IDE domains behave as three rigid bodies, IDE-N in two different
189 subunits within IDE dimer (IDE-N A, IDE-N B) and the dimeric IDE-C (IDE C/C). This is consistent with the
190 structural analysis of M16 family of metalloproteases (Liang *et al.*, 2022). This assertion is further supported
191 by our all-atom molecular dynamics (MD) simulations. While we observed small yet noticeable
192 conformational changes within IDE-N A, IDE-N B, and IDE-C/C, the overall RMSD of entire IDE dimer is
193 significantly higher than those three individual units (Fig. 3A). Multibody analysis defines the principal
194 components of variance along discrete eigenvectors, which we interpret as proxies for the dominant
195 components of molecular motion. We quantified the change in D1-D4 COM distance and D1-D2-D3-D4
196 COM dihedral of representative structures along the heterogeneity gradients of the top 9 eigenvectors for
197 each of our IDE structures, representing ~70-90% of the total structural heterogeneity per structure. The
198 results indicated that the particles comprising our cryo-EM structures sampled a significantly greater
199 conformational space than would be expected from analysis of the ensemble structures alone (Figure 3 -
200 figure supplement 2). Most intriguingly, the conformational changes displayed an unexpectedly high degree
201 of change in the D1-D2-D3-D4 COM dihedral angle, indicating a significant rotation of IDE-N relative to
202 IDE-C (Fig. 3B,C, Figure 3 – figure supplement 2).

203 Integration of the multibody results across all states of IDE suggest two dominant components of
204 structural variance. First is a translation-dominant conformational change wherein IDE-N swings toward or

205 away from IDE-C as if mediated by a hinge formed by the interdomain linker region of IDE (Fig. 3D, Figure
206 3 - video 1). This conformational change closely resembles our understanding of the IDE open-closed
207 transition inferred from analysis of the ensemble structures. The second component is a rotation-dominant
208 conformational change wherein IDE-N rotates orthogonal to the plane of the dimer as if it were being
209 screwed into or ground against IDE-C (Fig. 3E, Figure 3 – video 2). Importantly, these dominant
210 components of structural variance were also observed when the particle populations were analyzed with
211 cryoSPARC's 3DVA implementation, albeit over a smaller magnitude of conformational change (Figure 3 –
212 figure supplement 3). These dominant components also correlate well with the lowest frequency modes
213 revealed by normal mode analysis (Figure 3 – videos 3, 4). Interestingly, while the presence of insulin was
214 found to substantially influence the consensus reconstructions of IDE, we found that the presence or
215 absence of insulin had no significant effect on the principal components of structural variance for IDE,
216 consistent with the current understanding that enzyme conformational changes are "hardwired" into the
217 structure (Bahar *et al*, 2007; Bahar & Rader, 2005).

218 **R668 plays a key role in the IDE open/close transition in all-atom MD simulations**

219 Analysis of the particle heterogeneity comprising cryo-EM structures provides excellent information
220 about the conformational space sampled by the protein of interest. However, such analysis lacks a temporal
221 component, and thus only implies motions. To overcome this barrier and examine how the conformation of
222 IDE changes over time, we performed six replicate all-atom MD simulations with explicit solvent.
223 Simulations were initialized from the O/pO state (PDB: 7RZG), with the missing loops modeled in to
224 generate continuous peptide chains and run for one microsecond each. By starting with the O/pO structure,
225 we investigated the dynamics of both the open and closed subunits simultaneously. We observed that the
226 conformational space sampled by our simulations correlated well with the conformational space sampled
227 by our cryo-EM particle population, as revealed by multibody analysis (Figure 4 – figure supplement 1). In
228 5 of our 6 simulations, the open subunit closed quickly, typically in <200 ns (Fig. 4A). Analysis of the open-
229 close transition revealed two key findings. First, the open subunits did not close to a singular structure. We
230 define closing as a subunit reaching a similar D1-D4 COM distance as the pO or pC states, but we observed
231 distinct differences among the subunits indicative of IDE-N rotation relative to IDE-C. These differences are
232 in line with our second key finding, that the conformational changes associated with the open-close
233 transition did not follow the same general pathway among the simulations, as we observed a high degree
234 of variability upon closing (Fig. 4B).

235 Noticeably, R668 consistently stood out as one of the first IDE-C residues to form new interactions
236 with IDE-N, either D309 or E381 despite the path variation among our MD simulations (Fig. 4C). In most
237 simulations, formation of this interaction preceded a large decrease in the D1-D4 COM distance (Fig. 4D,
238 Figure 4 – figure supplement 2). Interestingly, these R668 interactions are not present in the ensemble
239 cryo-EM or crystal structures of IDE. We hypothesize that the biochemical properties and spatial localization
240 of R668 enable it to essentially reach out and grab onto the N-domain, initiating the formation of a complex
241 hydrogen bonding network that drives the open-close transition towards completion. Previously published

242 hydrogen-deuterium exchange mass spectrometry (HDX-MS) data indicates that R668 is stabilized under
243 conditions that promote IDE closing, suggesting that R668 may function as a molecular latch (Fig. 4E)
244 (Zhang *et al.*, 2018).

245 To further probe the importance of R668, we ran 6 additional simulations with IDE carrying a R668
246 to alanine (R668A) point mutation under identical conditions as described previously. These simulations
247 displayed significantly altered dynamics when compared to the wild-type simulations. Notably, the R668A
248 mutant was found to close more slowly, and many simulations did not reach the D1-D4 COM distance
249 typified by a closed state structure, instead stabilizing with a significantly larger D1-D4 COM distance than
250 we had previously observed in our wild type (WT) simulations or our experimental structures (Fig. 4F). We
251 also observed that the R668A mutant preferentially sampled a subset of conformational space rarely
252 explored in our WT simulations and displayed significantly greater variation in the D1-D2-D3-D4 dihedral
253 angle (Fig. 4G). As a result of this increased rotational exploration, several of our R668A simulations closed
254 to a conformation where IDE-N is offset and rotated relative to IDE-C when compared to the experimentally
255 determined structures (Figure 4 – figure supplement 3). This altered conformation results in a structure
256 where IDE-N and IDE-C are fully engaged, but the offset produces a deceivingly high D1-D4 COM distance.
257 With this in mind, we sought to better understand the conformational dynamics of IDE in the closed state.

258 **R668A modulates IDE conformational dynamics *in vitro***

259 The R668A mutation was found to significantly alter the conformational dynamics of IDE's open-
260 close transition in our simulations (Fig. 4F, G), so we expressed and purified the R668A mutant to determine
261 if the changes predicted from our MD simulations resulted in altered enzymatic activity relative to WT.
262 Previous work has established that IDE adopts a dominant O/pO state in solution (Zhang *et al.*, 2018).
263 Consistent with our MD simulations, size-exclusion chromatography revealed that the R668A construct
264 eluted slightly earlier than WT IDE, suggesting that the R668A mutation induces a greater proportion of
265 molecules to adopt a more open conformation, possibly shifting to a dominant O/O state (Fig. 5A). Next,
266 we compared the enzymatic activity of the R668A and WT constructs using the fluorogenic substrate (7-
267 methoxycourmarin-4-yl)acetyl-RPPGFSAFK(2,4-dinitrophenyl)-OH (substrate V), a bradykinin mimetic
268 which has previously been used to characterize the enzymatic activity of IDE and related enzymes (King *et*
269 *al*, 2014; McCord *et al.*, 2013). We found that WT IDE has activity consistent with previously published data
270 (McCord *et al.*, 2013) and the R668A mutation produced a ~5-fold decrease in activity (Fig. 5B). ATP is
271 known to promote IDE degradation of small substrates, i.e. bradykinin, but not larger substrates, i.e. insulin
272 (33). Consistent with this observation, the addition of ATP increased the activity of both WT and R668A
273 constructs (Fig. 5B). We also tested if the R668A mutation would alter the degradation of larger, well-folded
274 substrates, using insulin in a direct competition assay. We found that, after accounting for the previously
275 observed 5x decrease in activity, insulin yielded an apparent K_i of ~8 nM for WT IDE, but this value was
276 reduced to ~52 nM for the R668A construct (Fig. 5C). Conversely, when Aβ(1-40), an unstructured
277 substrate, was tested in the same competition assay, we observed an apparent K_i of ~688 nM for WT IDE,
278 yet the R668A mutant did not exhibit a dose-dependent response to the presence of Aβ and the data could

279 not be fit to any kinetic equation (Fig. 5D). We then performed size exclusion chromatography-coupled
280 small-angle X-ray scattering (SEC-SAXS) for both constructs to ascertain if the observed differences in
281 enzymatic activity could be explained by altered biophysical properties. The WT scattering profile produced
282 an R_g of 49.4 +/- 0.9 Å, consistent with previous SEC-SAXS results (Fig. 5E, F) (Zhang *et al.*, 2018). The
283 R668A scattering profile produced an R_g of 54.7 +/- 0.4 Å, consistent with our SEC data that R668A mutant
284 has slightly larger hydrodynamic radius (Fig. 5A). Together, our data indicates that R668A mutation can
285 profoundly affect the conformational dynamics governing the open-closed transition, and that altered
286 conformational dynamics can alter enzymatic activity in a substrate-dependent manner.

287 **Charge-swapping at the IDE-N/C interface mediates conformational dynamics in the closed state**

288 The WT pO subunit remained closed throughout all simulations yet was found to initially relax to a
289 slightly more open state within the first 200 ns, roughly the same time frame it took the WT O subunit to
290 close (Fig. 6A) and, despite not opening, demonstrated a range of D1-D2-D3-D4 dihedral variation similar
291 to that of the O subunits (Fig. 6B). Interestingly, the conformational variation within our simulations
292 increased greatly after this relaxation point was reached (Fig. 6A). This relaxed conformational state
293 consistently displayed an altered IDE-N/C interface compared to the experimentally determined structures
294 that was replicated by the open WT subunits upon closing, leading to a nearly symmetric pO/pO state
295 (Figure 6 – figure supplement 1). Biochemically, this relaxed IDE-N/C interface makes more sense than the
296 interface observed experimentally. It has previously been demonstrated that the experimental constraints
297 of crystallographic structure determination force IDE to adopt a closed conformation and determination of
298 the open state can only be accomplished once those restraints are removed, i.e. cryo-EM (Zhang *et al.*,
299 2018). These results suggest that both ensemble methods of structure determination may impact the
300 conformation of IDE, however slightly. The IDE-N/C interface is littered with charged residues, yet few
301 interactions are observed in the ensemble structures (Fig. 6C), whereas our MD simulations reveal a
302 complex hydrogen bonding network (Fig. 6D). We observed an extensive network at the D2-D3 interface,
303 with sporadic patches of interactions between D1 and D4 (Figure 6 – figure supplement 2). Within the D2-
304 D3 network R668 again stands out as a notably key residue. In addition to forming hydrogen bonds with
305 D309 and E381, we observed R668 form π-π interactions with R311 (Fig. 6E). Arginine-mediated π-
306 interactions have been well characterized in other systems for their ability to stabilize interaction interfaces
307 and facilitate conformational changes (Armstrong *et al*, 2016; Vernon *et al*, 2018).

308 The IDE-N/C interactions we observe in our simulations are not restricted to discrete cognate pairs;
309 rather, we observed that residues within the network periodically swap among several interaction partners.
310 This "charge-swapping" phenomenon allows IDE-N to rotate or slide against IDE-C to adopt multiple
311 conformations and maintain favorable interacting contacts (Fig. 6F). While multiple, concurrent, instances
312 of charge-swapping were associated with rapid changes in the D1-D2-D3-D4 dihedral angle, singular
313 events of charge-swapping did not appear to be significant enough to stimulate large-scale conformational
314 change (Fig. 6G, H). Instead, substantial conformational changes appear to be caused by multiple charge-
315 swapping events occurring in conjunction. This may explain why we observed no noticeable change in the

316 conformational dynamics of the pO state subunits when comparing the WT and R668A constructs. Consurf
317 analysis reveals that most of the residues forming these interaction networks are highly conserved among
318 IDE homologs (Figure 6 – figure supplement 3) (Ben Chorin *et al*, 2020). This indicates that the revealed
319 rotational motion is likely evolutionarily conserved and offers a potential mechanism by which IDE unfolds
320 and repositions bound peptide substrates to degrade amyloid peptides.

321 **Time-resolved cryo-EM suggests insulin-induced allostery in IDE**

322 To begin understanding of how the interaction between IDE and insulin leads to insulin unfolding
323 and degradation, we first performed all-atom MD simulation of insulin-bound IDE in the closed state.
324 Unfortunately, we did not observe a noticeable structural change of insulin within our microsecond
325 simulations. Previously, we used time-resolved SAXS analysis to determine the time constant for the insulin
326 induced open to closed transition, tau (τ, a.k.a., monoexponentially decay) to be ~100 milliseconds (Zhang
327 *et al.*, 2018). However, it has previously been determined that IDE cleaves about 2 insulin molecules every
328 second (Manolopoulou *et al.*, 2009). We employed spotiton to rapidly mix and freeze grids where IDE has
329 been exposed to insulin for 123 milliseconds prior to freezing (Dandey *et al*, 2020). We hoped that such an
330 experimental setup would permit the identification of novel insulin-bound states of IDE and offer insight into
331 the initial binding and unfolding of insulin. Previous work has established that, in the absence of substrate,
332 IDE adopts a dominant O/pO state in solution and the presence of a molar excess of substrate shifts the
333 particle population to a dominant pC/pC state (Zhang *et al.*, 2018). Surprisingly, after processing the dataset
334 in Relion, we observed a single conformational state within our rapidly-mixed dataset: the O/O state (Fig.
335 7A, Figure 7 - figure supplement 1, supplementary file 2). We were unable to resolve the structure beyond
336 moderate resolution (~5.1 Å) and did not observe unambiguous density indicative of insulin binding within
337 the catalytic chamber, which is unsurprising given our previous observations of promiscuous binding (Fig.
338 2C). Despite the relatively high particle number in our final reconstruction, we were unable to sub-classify
339 distinctly different conformations of IDE within the particle population as initial classes converged back to
340 the dominant O/O state upon subsequent refinement. This leads us to believe that the obtained O/O state
341 represents the average state of a particle population that exhibits a high degree of continuous structural
342 heterogeneity. The O/O state observed in our rapidly-mixed dataset is distinct from the previously observed
343 O/O states with D1-D4 center of mass distances of 55.1 Å and 46.8 Å matching the largest and smallest,
344 respectively, distances previously observed for individual O state subunits (Fig. 7B). The discrepancy
345 between the "openness" of the two subunits nearly doubles that observed in previous structures, making
346 this O/O state the most asymmetric O/O state yet observed (Fig. 7C). The observation of a dominant O/O
347 state in the presence of insulin under short timescales suggests that the binding of insulin to the O subunit
348 of the apo-dominant O/pO state can induce the pO state to open through an unknown allosteric mechanism
349 to reach the observed dominant O/O state (Fig. 7D). Positive allostery in IDE has previously been identified
350 in biochemical assays, yet we lack a detailed understanding of the underlying mechanism (McCord *et al.*,
351 2013; Song *et al*, 2011).

352 **Coarse-grained MD simulations reveal intermolecular cross-β sheet formation between insulin and**
353 **IDE in all four IDE domains**

354 As cryo-EM proved unsuitable to explore the mechanism of insulin unfolding by IDE, we turned to
355 MD simulations. As stated above, there is a notable discrepancy in the time frame between the open/close
356 transition and insulin cleavage rate. This suggests that unfolding requires multiple cycles of the open-closed
357 transition and, thus it is not currently realistic to use all-atom MD simulations to probe the unfolding of insulin
358 by IDE. We then used a coarse-grained MD package, Upside, to probe the interaction between IDE and
359 insulin. Upside performs the dynamics simulation for just 6 atoms per residue with the sidechains being
360 represented by directional-dependent beads whose packing probabilities have the lowest free energy while
361 still including key structure details to compute realistic forces (Faruk *et al*, 2022; Faruk *et al*, 2023; Jumper
362 *et al*, 2018a, b). This allows rapid equilibration and sampling of the energy landscape when compared with
363 the conventional all-atom MD simulation, achieving ~10^4 acceleration for the calculation time. Consistent
364 with all-atom MD simulations, Upside simulations revealed the wide range of motions, including grid and
365 hinge motions found in our all-atom MD simulation (Figure 8 – figure supplement 1). We observed the
366 partial unfolding of insulin in our Upside simulations yet, importantly, the unfolding did not disrupt the inter-
367 or intra-molecular disulfide bonds (Figure 8 video 1).

368 As insulin partially unfolds, it readily adopts β-strand structures—a key characteristic of
369 amyloidogenic peptides—which can transiently form cross-β-sheets with the central β-sheet present in all
370 four domains of IDE (Figure 8A-B). Specifically, we observed that cross-β-sheet interactions occur at
371 distinct regions of insulin: the N-terminus of insulin chain A interacts with the IDE D2 domain near the
372 substrate N-terminal anchoring site (also known as the exosite); the middle portion of insulin chain A
373 interacts with the IDE D1 domain; and the C-terminal regions of insulin chain B interact with the D3 and D4
374 domains of IDE. While the interactions of insulin with IDE-C domain are novel, those with IDE D1/D2
375 domains are structurally similar to those previously observed (Guo *et al*, 2010; Manolopoulou *et al.*, 2009;
376 Ren *et al*, 2010; Shen *et al.*, 2006). The labile and transient β-strand-rich interactions have been shown to
377 mediate diverse protein-protein interactions, e.g., the assembly of intermediate filaments (Eibauer *et al*,
378 2024; Zhou *et al*, 2021).

379 This interaction provides molecular insight into how IDE recognizes and binds amyloidogenic
380 peptides with diverse sequences (Figure 8C). IDE is capable of forming cross-β interactions with many
381 regions of insulin, primarily mediated by backbone-to-backbone contacts that do not rely on specific amino
382 acid sequences. The structural arrangement of IDE's four conserved domains enables it to interact with
383 multiple regions of its substrates, such as insulin, which are predisposed to forming β-strands (Figure 8C).
384 We term this type of interaction "β-grabbing," and propose that it is a key mechanism by which IDE unfolds
385 insulin. This interaction effectively tethers the substrate to both the IDE-N and IDE-C domains, facilitating
386 the interdomain motions of IDE that promote substrate unfolding.

387 **Discussion**

388 Our results allow us to put forth a refined model describing how IDE recognizes amyloid peptides
389 that are diverse in size and shape (Fig. 9). The catalytic cycle of IDE starts with at least one subunit of
390 dimeric IDE adopting the open state, exposing the interior of the catalytic chamber to potential substrates
391 (Zhang *et al.*, 2018). The unconstrained motion of IDE-N likely facilitates substrate interaction in a variety
392 of initial orientations. IDE-N and IDE-C have negatively and positively charged surfaces, respectively, and
393 are able to attract peptide substrates with complementary charge profiles (Shen *et al.*, 2006; Zhang *et al.*,
394 2018). Such peptides have a high dipole moment and are often prone to aggregation. However, in the open
395 state, the door subdomain, which contains the key catalytic residues, is highly flexible, rendering the open
396 state catalytically incompetent (McCord *et al.*, 2013; Zhang *et al.*, 2018). Proper positioning and unfolding
397 of substrate is necessary to stabilize the cleft prior to catalysis. Substrate binding has been suggested to
398 enhance IDE closing through charge complementarity (Shen *et al.*, 2006). It is likely that the rotation of IDE-
399 N permits a range of closing pathways to accommodate non-optimal substrate binding geometry (Fig. 4). If
400 the closing geometry permits R668 to interact with E381 or D309, the closing reaction continues to
401 completion. If the closing geometry does not permit the R668-mediated interactions, this could be a signal
402 of improper substrate binding, allowing IDE-N to open and either release improper substrate or reposition
403 for another closing attempt. Once closed, IDE-N is capable of rotating against IDE-C mediated by charge-
404 swapping events at the IDE-N/C interface (Fig. 6). The combined motions associated with the open to
405 closed transition and rotation between IDE-N and IDE-C can lead to the distortion of the secondary structure
406 of bound substrate. Furthermore, the transient interaction of insulin with the catalytic chamber of IDE such
407 as β-grabbing via the β–strand pairing should further stress the integrity of bound substrate (Fig. 8).
408 Together, these forces should facilitate unfolding and proper positioning of substrate for cleavage. Our data
409 indicates that IDE is able to accommodate any possible orientation of insulin tethering within the catalytic
410 site (Fig. 2C), suggesting that IDE is able to cut both chains of insulin in rapid succession without requiring
411 significant repositioning (Manolopoulou *et al.*, 2009). IDE then opens to release cleavage products and the
412 cycle begins anew.

413 IDE utilizes both unfoldase and protease activities to degrade clinically-relevant peptides, including
414 three glucose-regulating hormones with contrary effects – insulin, amylin, and glucagon – and Aβ, the
415 accumulation of which is associated with the progression of Alzheimer's disease. This has made IDE an
416 attractive target for therapeutic intervention (Maianti *et al.*, 2019; Tang, 2016). One major challenge is how
417 to better control selectivity when the substrates IDE degrades are highly diverse in sequence and structure.
418 It remains unknown how IDE unfolds substrates prior to cleavage. Our studies characterize the
419 conformational dynamics of IDE and offer insight into the catalytic mechanisms, revealing that IDE-N rotates
420 against IDE-C. We envision that this motion works in concert with the open-close transition to reposition
421 and unfold substrates prior to cleavage. This rotation appears to be largely unconstrained in the open state
422 and may play a role in promoting substrate capture. In the closed state, we found the rotational motion to
423 be mediated by charge-swapping events at the IDE-N/C interface. These events are supplemented by
424 interactions between hydrophobic patches that provide a non-specific interaction interface and allow the
425 domains to slide against one another. We found that IDE-N/C interactions were mediated by the key residue

426 R668, and mutation of this residue altered the enzymatic activity and conformation of IDE, likely by impairing
427 the open-close transition. Our data suggests that, while the R668A mutation globally impaired IDE activity,
428 R668A exhibits significantly different kinetic profiles towards well-folded substrates (insulin) compared to
429 unstructured substrates (Aβ). This highlights the complexity of the IDE catalytic cycle as we envision that
430 IDE conformational dynamics can regulate solvent access to the catalytic chamber and substrate binding,
431 unfolding, and cleavage are all intimately linked.

432 Our work adds to the expanding body of literature that integrates computational and experimental
433 approaches (Arenz *et al*, 2016; Hirschi *et al*, 2021; Jiang & Doudna, 2017; Palermo *et al*, 2016; Roh *et al*,
434 2020; Saha *et al*, 2022). By employing multibody analysis, we identified the dominant sources of structural
435 heterogeneity within our cryo-EM particle population, uncovering that the conformational dynamics of IDE
436 involve a substantial rotational component that is not evident from ensemble structure analysis alone. We
437 showed that all-atom MD simulations can address limitations of cryo-EM single particle analysis when
438 investigating the role of residue R668. Because R668 forms a network of polar and electrostatic interactions
439 rather than exclusive partnerships, dynamic hydrogen bonding networks at the IDE-N/C interface—
440 particularly those involving R668—contribute to conformational heterogeneity, which further restricts the
441 achievable resolution in cryo-EM analysis. Furthermore, vitrification by freezing proteins in liquid ethane
442 can significantly alter the entropic contribution of R668 through conformation-dependent promiscuous
443 contacts. By combining cryo-EM and MD simulations, we gained insight into how flexible interactions
444 between IDE-N and IDE-C facilitate domain movements and highlighted the critical role of R668 in
445 mediating these interactions. We also used MD simulations to demonstrate altered open-closed dynamics
446 in the R668A mutant compared to the wild-type enzyme and validated these findings with experimental
447 enzymatic kinetic assays and SEC-SAXS experiments.

448 At its core, cryo-EM is an ensemble method of structure determination, averaging tens of thousands
449 of particles together to generate consensus structures. While methodologies have been well-established to
450 separate out discrete conformational classes, proteins that exhibit constant gradients of structural
451 heterogeneity remain problematic, although significant attention has been devoted to the issue in recent
452 years, with varying levels of success (Nakane *et al.*, 2018; Punjani & Fleet, 2021; Zhong *et al*, 2021).
453 Currently, the best approaches use various dimensionality reduction techniques to analyze the principal
454 components of particle heterogeneity. While a substantial innovation, it remains to be seen how the principal
455 components of structural heterogeneity, derived from a series of static snapshots of a particle at the time
456 of freezing, correlate with the real molecular motions of a protein in an aqueous environment. For many
457 systems, especially enzymes of clinical significance, proper characterization of the conformational
458 dynamics and transitional states of the protein are necessary for a full understanding of protein function
459 and lays the foundation for future therapeutic development. MD simulations can provide this information,
460 yet such studies are often met with skepticism by experimental researchers. By integrating MD simulations
461 with experimental techniques, the weaknesses of one technique can be compensated for by the strengths
462 of other techniques to provide comprehensive information about the system of interest. While this

463 integrative approach has proven beneficial across a wide range of systems, including proteorhodopsin, the
464 ribosome, and rotary ATPases, perhaps the best example of this approach is the CRISPR-Cas9 system,
465 where an exhaustive number of studies have combined cryo-EM, crystallography, and traditional
466 biophysical techniques with traditional and accelerated MD methods to drive the field forward at an
467 astounding pace (Arenz *et al.*, 2016; Hirschi *et al.*, 2021; Jiang & Doudna, 2017; Palermo *et al.*, 2016; Roh
468 *et al.*, 2020; Saha *et al.*, 2022).

469 Our integrative structural analyses provide the structural basis for IDE conformational dynamics
470 and their roles in IDE catalytic cycle and the framework for future studies. We speculate that multi-cycles
471 of open-close transition and rotation driven by IDE conformational dynamics will be required for its
472 unfoldase activity. However, the kinetic timescale of this reaction is fast, estimated to be ~500 milliseconds
473 rendering investigation challenging experimentally while the timescale is long for all-atom MD simulation
474 (Manolopoulou *et al.*, 2009). Our cryo-EM analyses also shed light on IDE allostery (McCord *et al.*, 2013;
475 Song *et al.*, 2011; Zhang *et al.*, 2018) (Fig. 9). The IDE dimer primarily adopts the O/pO conformational
476 state (Zhang *et al.*, 2018). Through time-resolved cryo-EM analysis, our data suggest that, upon substrate
477 binding to the O state, the substrate-inaccessible pO state undergoes allosteric opening, allowing this
478 subunit to capture its substrate. Additionally, the prolonged incubation of IDE with sub-stoichiometric
479 amounts of insulin results in the predominance of the pC/pC state, suggestive of coordination in substrate
480 capture and open-closed transition. Collectively, these positive allosteric transitions would enhance IDE's
481 capacity to capture and degrade its substrates more efficiently, though the underlying mechanisms remain
482 unclear. Future integrative structural studies are required to further elucidate and control the IDE catalytic
483 cycle, enabling substrate-specific modulation of IDE activity and advancing its therapeutic potential.

484 **Materials and Methods**

485 Expression and purification of human IDE:

486 Cysteine-free IDE (referred to as IDE in this study) was expressed in *E. coli* BL21 (DE3) cells (at
487 25 °C for 20 h, 0.5mM IPTG induction using T7 medium). The R668A mutation was introduced into this
488 construct by site-directed mutagenesis with the following primer pair:
489 CCGGAAATTGTTAAGAGATGCCATATATGCTTCTTTG (forward)
490 CAAAGAAGCATATATGGCATCTCTTAACAACCGGGC (reverse) and verified by sequencing.
491 Recombinant IDE proteins were purified by Ni-NTA, source-Q, and Superdex 200 columns as previously
492 described (Zhang *et al.*, 2018). Protein was aliquoted and stored at -80° C.
493

494 Cryo-EM data collection and analysis:

495 Thawed IDE aliquots were further purified by Superdex 200 chromatography using buffer
496 containing 20 mM HEPES, pH 7.2, 150 mM NaCl, 10mM EDTA and then mixed with Fab_{H11-E} at an equal
497 molar ratio. Fab_{H11-E}-IDE complex was purified by Superdex 200 chromatography in the presence of insulin
498 at molar ratio IDE:insulin=2:1. Insulin was purchased from SIGMA (91077C). All grids, 300 mesh carbon or
499 gold holey nanowire grids were plasma cleaned with O_2 and H_2 for 10 secs using a Solarus plasma cleaner

500 (Gatan) and plunged at 133 milli-second using Chameleon, Spotiton-based technology. All images were
501 acquired using a Titan Krios microscope (FEI) operated at 300KeV with a Gatan K3 direct electron detector
502 (Gatan) in counting mode. Images were automatically acquired using Leginon (Suloway *et al*, 2005).
503 Images were processed using software integrated into RELION3 (Zivanov *et al*, 2018). Frames were
504 aligned using MotionCor2 (Zheng *et al*, 2017) software with dose weighting, CTF was estimated using Gctf
505 (Zhang, 2016), particles were picked and extracted automatically using RELION. Particle stacks were
506 processed through several rounds of 2D and 3D classification. Selected classes were then processed for
507 high-resolution 3D refinement. The flowchart and detailed data processing is summarized in Figure 2 figure
508 supplement 1. Finally, the overall map was improved by particle polishing in RELION and sharpening. The
509 final resolution was estimated using Fourier Shell Correlation (FSC=0.143, gold-standard). The density
510 fitting and structure refinement was done using UCSF CHIMERA (Pettersen *et al*, 2004), COOT (Emsley &
511 Cowtan, 2004), REFMAC5 (Murshudov *et al*, 2011) and PHENIX (Adams *et al*, 2010). Time-resolved cryo-
512 EM grids by rapidly mixing IDE+Fab with insulin were prepared using the Spotiton device as previously
513 described (Budell *et al*, 2021; Dandey *et al.*, 2020). In brief, IDE+fab and insulin were thawed on ice and
514 diluted in 20 mM HEPES, pH 7.2, 150 mM NaCl, 10 mM EDTA to 25 μM and 127.5 μM, respectively. Self-
515 wicking, nanowire grids were plasma treated (Gatan Solarus) at 5 W in hydrogen and oxygen for 1-2
516 minutes (Wei *et al*, 2018). Each sample was aspirated into separate piezodispensers and applied
517 sequentially in 70-100% relative humidity at 22-25C onto plunging grids just before cryogen entry. The
518 maximum constant velocity of the plunging robot was adjusted to obtain the target sample mixing times of
519 123 milliseconds. The data was collected and processed as above, in Relion5, with Blush regularization
520 being employed during 3D refinement.

521 <u>Multibody analysis:</u>

522 We defined three rigid bodies as shown in figure 2A for the analysis. The size of the user-defined
523 bodies has been theorized to play a significant role in the success of multibody refinement, most likely due
524 to the fact that larger bodies will have a stronger signal-to-noise ratio (Nakane *et al.*, 2018). With a Fab
525 bound to each of IDE-N within IDE dimer, we assessed the impact of body size on multibody refinement by
526 examining how density corresponding to 2 F_v regions, 1 F_v region, or no F_v regions would affect the
527 multibody refinement. Fab has a variable region (F_v), and a constant region (F_c) and we chose to subtract
528 and mask out the density corresponding to the Fab F_c, as we speculated that any motion between the Fab
529 F_v and F_c domains would bias the results of the multibody refinement. The quality of the multibody results
530 was assessed based on the subsequent improvement in the Coulomb potential map quality and calculated
531 resolution. In the absence of any F_v density, the maps resulting from multibody refinement had the best
532 calculated resolution, yet the map quality was quite poor overall; much of the density appears globular and
533 featureless, particularly in the IDE-N regions (Figure 2 – figure supplement 4). Conversely, when F_v density
534 was present on both IDE-N bodies, the resolution of the multibody output maps (4.5 Å) was worse than the
535 resolution of the input map (4.3 Å). Thus, we found that the greatest improvement occurred when the F_v

536 density was present on only the exterior body of the pO subunit. In this case, multibody refinement improved
537 both the calculated resolution and density quality.

538 Following multibody refinement, the structural heterogeneity for each body was analyzed along six
539 principal component vectors, resulting in 18 vectors describing the primary components of structural
540 variation within the IDE dimer. We analyzed the variation along these vectors as a proxy for protein motion.
541 The results of the multibody analysis indicate the degree of structural variation that is explained by motion
542 along each of the primary component vectors. For all IDE states, we observed no single component vector
543 could explain the majority of structural variance (Supplementary files 3-8). Given the underlying
544 assumptions of multibody refinement, there is a question of whether any observed motions are biologically
545 relevant or simply the result of improper particle alignment. We reasoned that the greater the degree of
546 variation explained by motion along a specified component vector, the greater the likelihood was that the
547 motion would be biologically relevant. Therefore, we focus on the top 9 component vectors, which cover
548 ~75% of total variance for each state, in greater detail.

549 Molecular dynamics simulations:

550 All-atom MD simulations were prepared from the O/pO structure of IDE (PDB: 7RZK) and
551 necessary CHARMM force field PARAM36 files using QwikMD (Ribeiro *et al*, 2016). Gaps in the structure
552 were modeled in using the AlphaFold model of IDE. A three-step minimization-annealing-equilibration
553 process was used to generate an equilibrated system. Simulations were performed under NPT (constant
554 numbers of particles N, pressure P, and temperature T) conditions at 310 K and 1 atm with periodic
555 boundary conditions in NAMD3.0 (Phillips *et al*, 2005). Explicit solvent was described with the TIP3P model
556 (Jorgensen *et al*, 1983). Custom TCL scripts in VMD were used to calculate the D1-D4 centers-of-mass
557 distance and D1-D2-D3-D4 centers-of-mass dihedral angle (Supplementary file 9). Residues 964-988 in
558 D4 that are mostly absence in all static structures of IDE were built using Alpha-fold, which is highly flexible
559 in our MD simulations. They were omitted from the analysis of MD simulations, as the inclusion of this
560 flexible loop significantly altered the center-of-mass independent of global conformational change.

561 Initial structure of insulin bound IDE, for Upside simulations, was generated using PYMOL that
562 started with IDE closed monomer (PDB code: 6BF8). Intact insulin (PDB code: 4INS) was fixed by mutation
563 of residue 30 of insulin chain B back to threonine and modeled into the catalytic chamber based on the
564 crystal structure of IDE in complex with the partially unfolded insulin (PDB code: 2WBY). The upside
565 simulation was run with 28 replicates at T_{Upside}=0.8 using Upside 1.0 force field parameters and our total
566 upside simulation time is approximately 28 μsec (Faruk *et al.*, 2022; Faruk *et al.*, 2023; Jumper *et al.*, 2018a,
567 b). We estimated Upside's time step to be ~0.1 picosecond based on folding rates and chain motions.
568 Custom R, and Python scripts were used for data analysis and presentation (Supplementary files 10-12).

569 Enzymatic assays:

570 IDE constructs were exchanged into activity buffer comprised of 25 mM Tris-HCl pH 7.5, 150 mM
571 NaCl, and 10 mM $ZnCl_2$. MCA-RPPGFSAFK(Dnp) was purchased from Enzo Life Sciences
572 (BMLP2270001), resuspended in dimethyl sulfoxide at a concentration of 5 mM and diluted to 5 μM with
573 activity buffer. For activity measurements, 5 μM MCA-RPPGFSAFK(Dnp) was mixed with the desired IDE
574 construct at concentrations ranging from 1-100 nM in the presence or absence of 1 mM ATP in a 200 μl
575 reaction. Fluorescence was monitored every 30 sec for 30 minutes with excitation/emission wavelengths of
576 320/405 nm at 37° C. Initial velocity was calculated during the linear range. Insulin was purchased from MP
577 Biomedicals (#0219390010), resuspended in 0.01N HCl at 1 mM and diluted to desired concentration with
578 activity buffer. For competition assays, 5 nM IDE construct and 5 μM MCA-RPPGFSAFK(Dnp) was mixed
579 with insulin ranging from 0-100 μM. Fluorescence was monitored every 30 sec for 30 minutes with
580 excitation/emission wavelengths of 320/405 nm at 37° C. Initial velocity was calculated during the linear
581 range for each concentration of insulin and normalized relative to the respective construct's velocity in the
582 absence of insulin to maintain consistency across plates, yielding values for relative inhibition which were
583 plotted vs [insulin] or [Aβ] and fit to the Michaelis-Menten equation in xmgrace to generate apparent K_i
584 values. All experiments were performed in triplicate.

585 Size-exclusion chromatography coupled small-angle X-ray scattering

586 SAXS/WAXS data collection was employed the Life Sciences X-ray Scattering (LIX) Beamline at
587 the National Synchrotron Light Source II (NSLS II) at Brookhaven National Laboratory in Upton, NY. Briefly,
588 60ul of samples in solution were pipetted into PCR tubes, placed into a Bio-Inert Agilent 1260 Infinity II
589 HPLC multisampler and measured using the isocratic SEC-SAXS format at the beamline (Yang *et al*, 2021).
590 50ul of sample was injected into the Phenomenex Biozen dSEC2 3 μm bead size with 200Å pore size
591 column was utilized at a flow rate of 0.35mL/min for 25 minutes. SAXS and WAXS data are collected
592 simultaneously on a Pilatus 1M (SAXS) and Pilatus 900K (WAXS) detectors with a 2 second exposure
593 (Yang *et al*, 2020). Data from both detectors is then scaled and merged. Intensity is normalized using the
594 water peak height at 2.0 $Å^{-1}$. Data processing and analysis was performed using py4xs and lixtools in
595 jupyter lab. Buffer frames 100-125 were averaged and used for subtraction of averaged frames under the
596 peak of interest.

597 **Data Availability**

598 Cryo-EM maps and refined models have been deposited to the EMDB and PDB, respectively with the
599 following accession numbers:

600 O/O state: EMDB-24760, PDB 7RZH

601 O/pO state: EMDB-24759, PDB 7RZG

602 pO/pC state: EMDB-24757, PDB 7RZE

603 O/pC state: EMDB-24758, PDB 7RZF

604 pC/pC state: EMDB-24761, PDB 7RZI

605 Time-resolved O/O state: EMDB-72393, PDB 9Y0H

606 Cryo-EM micrographs have been deposited to the Electron Microscopy Public Image Archive (EMPIAR)
607 under the following accession numbers:

608 IDE+insulin in a 2:1 ratio: EMPIAR-11610

609 Time-resolved IDE+insulin: EMPIAR-12968.

610 **References**

611 Adams PD, Afonine PV, Bunkoczi G, Chen VB, Davis IW, Echols N, Headd JJ, Hung LW, Kapral GJ, Grosse-
612 Kunstleve RW *et al* (2010) PHENIX: a comprehensive Python-based system for macromolecular structure
613 solution. *Acta Crystallogr D Biol Crystallogr* 66: 213-221
614 Arenz S, Bock LV, Graf M, Innis CA, Beckmann R, Grubmüller H, Vaiana AC, Wilson DN (2016) A combined
615 cryo-EM and molecular dynamics approach reveals the mechanism of ErmBL-mediated translation
616 arrest. *Nature Communications* 7: 12026
617 Armstrong CT, Mason PE, Anderson JLR, Dempsey CE (2016) Arginine side chain interactions and the role
618 of arginine as a gating charge carrier in voltage sensitive ion channels. *Scientific Reports* 6: 21759
619 Bahar I, Chennubhotla C, Tobi D (2007) Intrinsic dynamics of enzymes in the unbound state and, relation
620 to allosteric regulation. *Current opinion in structural biology* 17: 633-640
621 Bahar I, Rader AJ (2005) Coarse-grained normal mode analysis in structural biology. *Current opinion in*
622 *structural biology* 15: 586-592
623 Baker EN, Blundell TL, Cutfield JF, Cutfield SM, Dodson EJ, Dodson GG, Hodgkin DMC, Hubbard RE, Isaacs
624 NW, Reynolds CD *et al* (1988) The Structure of 2zn Pig Insulin Crystals at 1.5-a Resolution. *Philosophical*
625 *Transactions of the Royal Society B-Biological Sciences* 319: 369-456
626 Ben Chorin A, Masrati G, Kessel A, Narunsky A, Sprinzak J, Lahav S, Ashkenazy H, Ben-Tal N (2020)
627 ConSurf-DB: An accessible repository for the evolutionary conservation patterns of the majority of PDB
628 proteins. *Protein Science* 29: 258-267
629 Bertram L, Blacker D, Mullin K, Keeney D, Jones J, Basu S, Yhu S, McInnis MG, Go RC, Vekrellis K *et al*
630 (2000) Evidence for genetic linkage of Alzheimer's disease to chromosome 10q. *Science* 290: 2302-2303
631 Bertram L, McQueen MB, Mullin K, Blacker D, Tanzi RE (2007) Systematic meta-analyses of Alzheimer
632 disease genetic association studies: the AlzGene database. *Nat Genet* 39: 17-23
633 Budell WC, Allegri L, Dandey V, Potter CS, Carragher B (2021) Cryo-Electron Microscopic Grid
634 Preparation for Time-Resolved Studies using a Novel Robotic System, Spotiton. *Jove-Journal of Visualized*
635 *Experiments*
636 Busto-Moner L, Feng CJ, Antoszewski A, Tokmakoff A, Dinner AR (2021) Structural Ensemble of the
637 Insulin Monomer. *Biochemistry* 60: 3125-3136
638 Charton J, Gauriot M, Guo Q, Hennuyer N, Marechal X, Dumont J, Hamdane M, Pottiez V, Landry V,
639 Sperandio O *et al* (2014) Imidazole-derived 2-[N-carbamoylmethyl-alkylamino]acetic acids, substrate-
640 dependent modulators of insulin-degrading enzyme in amyloid-β hydrolysis. *Eur J Med Chem* 79: 184-
641 193

642 Chiti F, Dobson CM (2006) Protein misfolding, functional amyloid, and human disease. *Annual review of*
643 *biochemistry* 75: 333-366
644 Chiti F, Dobson CM (2017) Protein Misfolding, Amyloid Formation, and Human Disease: A Summary of
645 Progress Over the Last Decade. *Annual review of biochemistry* 86: 27-68
646 Dandey VP, Budell WC, Wei H, Bobe D, Maruthi K, Kopylov M, Eng ET, Kahn PA, Hinshaw JE, Kundu N *et*
647 *al* (2020) Time-resolved cryo-EM using Spotiton. *Nature Methods* 17: 897-900
648 Eibauer M, Weber MS, Kronenberg-Tenga R, Beales CT, Boujemaa-Paterski R, Turgay Y, Sivagurunathan
649 S, Kraxner J, Köster S, Goldman RD *et al* (2024) Vimentin filaments integrate low-complexity domains in
650 a complex helical structure. *Nature Structural & Molecular Biology* 31
651 Emsley P, Cowtan K (2004) Coot: model-building tools for molecular graphics. *Acta Crystallographica*
652 *Section D-Biological Crystallography* 60: 2126-2132
653 Farris W, Mansourian S, Chang Y, Lindsley L, Eckman EA, Frosch MP, Eckman CB, Tanzi RE, Selkoe DJ,
654 Guenette S (2003) Insulin-degrading enzyme regulates the levels of insulin, amyloid beta-protein, and
655 the beta-amyloid precursor protein intracellular domain in vivo. *Proc Natl Acad Sci USA* 100: 4162-4167
656 Farris W, Mansourian S, Leissring MA, Eckman EA, Bertram L, Eckman CB, Tanzi RE, Selkoe DJ (2004)
657 Partial loss-of-function mutations in insulin-degrading enzyme that induce diabetes also impair
658 degradation of amyloid beta-protein. *Am J Pathol* 164: 1425-1434
659 Faruk NF, Peng XD, Freed KF, Roux B, Sosnick TR (2022) Challenges and Advantages of Accounting for
660 Backbone Flexibility in Prediction of Protein-Protein Complexes. *Journal of Chemical Theory and*
661 *Computation* 18: 2016-2032
662 Faruk NF, Peng XD, Sosnick TR (2023) Factors That Control the Force Needed to Unfold a Membrane
663 Protein in Silico Depend on the Mode of Denaturation. *International Journal of Molecular Sciences* 24
664 Greenwald J, Riek R (2010) Biology of amyloid: structure, function, and regulation. *Structure* 18: 1244-
665 1260
666 Guo Q, Manolopoulou M, Bian Y, Schilling AB, Tang WJ (2010) Molecular basis for the recognition and
667 cleavages of IGF-II, TGF-alpha, and amylin by human insulin-degrading enzyme. *J Mol Biol* 395: 430-443
668 Hipp MS, Kasturi P, Hartl FU (2019) The proteostasis network and its decline in ageing. *Nat Rev Mol Cell*
669 *Biol* 20: 421-435
670 Hirschi S, Kalbermatter D, Ucurum Z, Lemmin T, Fotiadis D (2021) Cryo-EM structure and dynamics of
671 the green-light absorbing proteorhodopsin. *Nature Communications* 12: 4107
672 Im H, Manolopoulou M, Malito E, Shen Y, Zhao J, Neant-Fery M, Sun CY, Meredith SC, Sisodia SS,
673 Leissring MA *et al* (2007) Structure of substrate-free human insulin-degrading enzyme (IDE) and
674 biophysical analysis of ATP-induced conformational switch of IDE. *J Biol Chem* 282: 25453-25463
675 Jiang FG, Doudna JA (2017) CRISPR-Cas9 Structures and Mechanisms. *Annual Review of Biophysics* 46:
676 505-529
677 Jorgensen WL, Chandrasekhar J, Madura JD, Impey RW, Klein ML (1983) Comparison of Simple Potential
678 Functions for Simulating Liquid Water. *Journal of Chemical Physics* 79: 926-935
679 Jumper JM, Faruk NF, Freed KF, Sosnick TR (2018a) Accurate calculation of side chain packing and free
680 energy with applications to protein molecular dynamics. *PLoS computational biology* 14: e1006342
681 Jumper JM, Faruk NF, Freed KF, Sosnick TR (2018b) Trajectory-based training enables protein
682 simulations with accurate folding and Boltzmann ensembles in cpu-hours. *PLoS computational biology*
683 14: e1006578
684 Kim M, Hersh LB, Leissring MA, Ingelsson M, Matsui T, Farris W, Lu A, Hyman BT, Selkoe DJ, Bertram L *et*
685 *al* (2007) Decreased catalytic activity of the insulin-degrading enzyme in chromosome 10-linked
686 Alzheimer disease families. *J Biol Chem* 282: 7825-7832
687 King JV, Liang WG, Scherpelz KP, Schilling AB, Meredith SC, Tang W-J (2014) Molecular Basis of Substrate
688 Recognition and Degradation by Human Presequence Protease. *Structure* 22: 996-1007

689 Leissring MA, Farris W, Chang AY, Walsh DM, Wu X, Sun X, Frosch MP, Selkoe DJ (2003) Enhanced
690 proteolysis of beta-amyloid in APP transgenic mice prevents plaque formation, secondary pathology,
691 and premature death. *Neuron* 40: 1087-1093
692 Li P, Kuo WL, Yousef M, Rosner MR, Tang WJ (2006) The C-terminal domain of human insulin degrading
693 enzyme is required for dimerization and substrate recognition. *Biochem Biophys Res Commun* 343:
694 1032-1037
695 Liang WG, Wijiya J, Wei H, Noble A, Mo S, Lee D, Mancl JM, King JL, Pan M, Liu C *et al* (2022) Structural
696 basis for the mechanisms of human presequence protease conformational switch and substrate
697 recognition. *Nature Communications* 13: 1833
698 Lopez-Otin C, Blasco MA, Partridge L, Serrano M, Kroemer G (2013) The hallmarks of aging. *Cell* 153:
699 1194-1217
700 Maianti JP, McFedries A, Foda ZH, Kleiner RE, Du XQ, Leissring MA, Tang W-J, Charron MJ, Seeliger MA,
701 Saghatelian A *et al* (2014) Anti-diabetic activity of insulin-degrading enzyme inhibitors mediated by
702 multiple hormones. *Nature* 511: 94-98
703 Maianti JP, Tan GA, Vetere A, Welsh AJ, Wagner BK, Seeliger MA, Liu DR (2019) Substrate-selective
704 inhibitors that reprogram the activity of insulin-degrading enzyme. *Nat Chem Biol* 15: 565-574
705 Malito E, Hulse RE, Tang WJ (2008) Amyloid β-degrading cryptidases: insulin degrading enzyme,
706 presequence peptidase, and neprilysin. *Cell Mol Life Sci* 65: 2574-2585
707 Manolopoulou M, Guo Q, Malito E, Schilling AB, Tang WJ (2009) Molecular basis of catalytic chamber-
708 assisted unfolding and cleavage of human insulin by human insulin-degrading enzyme. *J Biol Chem* 284:
709 14177-14188
710 McCord LA, Liang WG, Dowdell E, Kalas V, Hoey RJ, Koide A, Koide S, Tang W-J (2013) Conformational
711 states and recognition of amyloidogenic peptides of human insulin-degrading enzyme. *Proceedings of*
712 *the National Academy of Sciences of the United States of America* 110: 13827-13832
713 Murshudov GN, Skubák P, Lebedev AA, Pannu NS, Steiner RA, Nicholls RA, Winn MD, Long F, Vagin AA
714 (2011) REFMAC5 for the refinement of macromolecular crystal structures. *Acta Crystallographica*
715 *Section D-Structural Biology* 67: 355-367
716 Nakane T, Kimanius D, Lindahl E, Scheres SH (2018) Characterisation of molecular motions in cryo-EM
717 single-particle data by multi-body refinement in RELION. *Elife* 7: e36861
718 Palermo G, Miao YL, Walker RC, Jinek M, McCammon JA (2016) Striking Plasticity of CRISPR-Cas9 and Key
719 Role of Non-target DNA, as Revealed by Molecular Simulations. *Acs Central Science* 2: 756-763
720 Pettersen EF, Goddard TD, Huang CC, Couch GS, Greenblatt DM, Meng EC, Ferrin TE (2004) UCSF
721 chimera - A visualization system for exploratory research and analysis. *Journal of computational*
722 *chemistry* 25: 1605-1612
723 Phillips JC, Braun R, Wang W, Gumbart J, Tajkhorshid E, Villa E, Chipot C, Skeel RD, Kalé L, Schulten K
724 (2005) Scalable molecular dynamics with NAMD. *Journal of computational chemistry* 26: 1781-1802
725 Punjani A, Fleet DJ (2021) 3D variability analysis: Resolving continuous flexibility and discrete
726 heterogeneity from single particle cryo-EM. *Journal of Structural Biology* 213: 107702
727 Ren M, Guo Q, Guo L, Lenz M, Qian F, Koenen RR, Xu H, Schilling AB, Weber C, Ye RD *et al* (2010)
728 Polymerization of MIP-1 chemokine (CCL3 and CCL4) and clearance of MIP-1 by insulin-degrading
729 enzyme. *EMBO J* 29: 3952-3966
730 Ribeiro JV, Bernardi RC, Rudack T, Stone JE, Phillips JC, Freddolino PL, Schulten K (2016) QwikMD -
731 Integrative Molecular Dynamics Toolkit for Novices and Experts. *Scientific Reports* 6: 26536
732 Roh SH, Shekhar M, Pintilie G, Chipot C, Wilkens S, Singharoy A, Chiu W (2020) Cryo-EM and MD infer
733 water-mediated proton transport and autoinhibition mechanisms of V complex. *Science Advances* 6:
734 eabb9605
735 Saha A, Arantes PR, Palermo G (2022) Dynamics and mechanisms of CRISPR-Cas9 through the lens of
736 computational methods. *Current opinion in structural biology* 75: 102400

Saido T, Leissring MA (2012) Proteolytic degradation of amyloid beta-protein. *Cold Spring Harb Perspect Med* 2: a006379

Shen Y, Joachimiak A, Rosner MR, Tang WJ (2006) Structures of human insulin-degrading enzyme reveal a new substrate recognition mechanism. *Nature* 443: 870-874

Sladek R, Rocheleau G, Rung J, Dina C, Shen L, Serre D, Boutin P, Vincent D, Belisle A, Hadjadj S *et al* (2007) A genome-wide association study identifies novel risk loci for type 2 diabetes. *Nature* 445: 881-885

Song ES, Jang H, Guo HF, Juliano MA, Juliano L, Morris AJ, Galperin E, Rodgers DW, Hersh LB (2017) Inositol phosphates and phosphoinositides activate insulin-degrading enzyme, while phosphoinositides also mediate binding to endosomes. *Proceedings of the National Academy of Sciences of the United States of America* 114: E2826-E2835

Song ES, Juliano MA, Juliano L, Fried MG, Wagner SL, Hersh LB (2004) ATP effects on insulin-degrading enzyme are mediated primarily through its triphosphate moiety. *Journal of Biological Chemistry* 279: 54216-54220

Song ESE, Rodgers DWD, Hersh LBL (2011) Mixed dimers of insulin-degrading enzyme reveal a cis activation mechanism. *The Journal of biological chemistry* 286: 13852-13858

Suloway C, Pulokas J, Fellmann D, Cheng A, Guerra F, Quispe J, Stagg S, Potter CS, Carragher B (2005) Automated molecular microscopy: the new Leginon system. *J Struct Biol* 151: 41-60

Tang WJ (2016) Targeting Insulin-Degrading Enzyme to Treat Type 2 Diabetes Mellitus. *Trends Endocrinol Metab* 27: 24-34

Tanzi RE, Bertram L (2005) Twenty years of the Alzheimer's disease amyloid hypothesis: a genetic perspective. *Cell* 120: 545-555

Vernon RM, Chong PA, Tsang B, Kim TH, Bah A, Farber P, Lin H, Forman-Kay JD (2018) Pi-Pi contacts are an overlooked protein feature relevant to phase separation. *Elife* 7: e31486

Wei H, Dandey VP, Zhang ZN, Raczkowski A, Rice WJ, Carragher B, Potter CS (2018) Optimizing "self-wicking" nanowire grids. *Journal of Structural Biology* 202: 170-174

Yang L, Antonelli S, Chodankar S, Byrnes J, Lazo E, Qian K (2020) Solution scattering at the Life Science X-ray Scattering (LiX) beamline. *J Synchrotron Radiat* 27: 804-812

Yang L, Lazo E, Byrnes J, Chodankar S, Antonelli S, Rakitin M (2021) Tools for supporting solution scattering during the COVID-19 pandemic. *J Synchrotron Radiat* 28: 1237-1244

Zeggini E, Weedon MN, Lindgren CM, Frayling TM, Elliott KS, Lango H, Timpson NJ, Perry JRB, Rayner NW, Freathy RM *et al* (2007) Replication of genome-wide association signals in UK samples reveals risk loci for type 2 diabetes. *Science* 316: 1336-1341

Zhang K (2016) Gctf: Real-time CTF determination and correction. *Journal of Structural Biology* 193: 1-12

Zhang ZN, Liang WGG, Bailey LJ, Tan YZ, Wei H, Wang A, Farcasanu M, Woods VA, McCord LA, Lee D *et al* (2018) Ensemble cryoEM elucidates the mechanism of insulin capture and degradation by human insulin degrading enzyme. *Elife* 7: e33572

Zheng S, Polovcak E, Armache JP, Cheng Y, Agard D (2017) MotionCor2: anisotropic Correction of Beam-induced Motion for Improved Single-particle Electron Cryomicroscopy. *Nature Methods* 14: 331-332

Zhong ED, Bepler T, Berger B, Davis JH (2021) CryoDRGN: reconstruction of heterogeneous cryo-EM structures using neural networks. *Nature Methods* 18: 176-185

Zhou XM, Lin Y, Kato M, Mori E, Liszczak G, Sutherland L, Sysoev VO, Murray DT, Tycko R, McKnight SL (2021) Transiently structured head domains control intermediate filament assembly. *Proceedings of the National Academy of Sciences of the United States of America* 118

Zivanov J, Nakane T, Forsberg BO, Kimanius D, Hagen WJ, Lindahl E, Scheres SH (2018) New tools for automated high-resolution cryo-EM structure determination in RELION-3. *Elife* 7: e42166

784 **Figures**

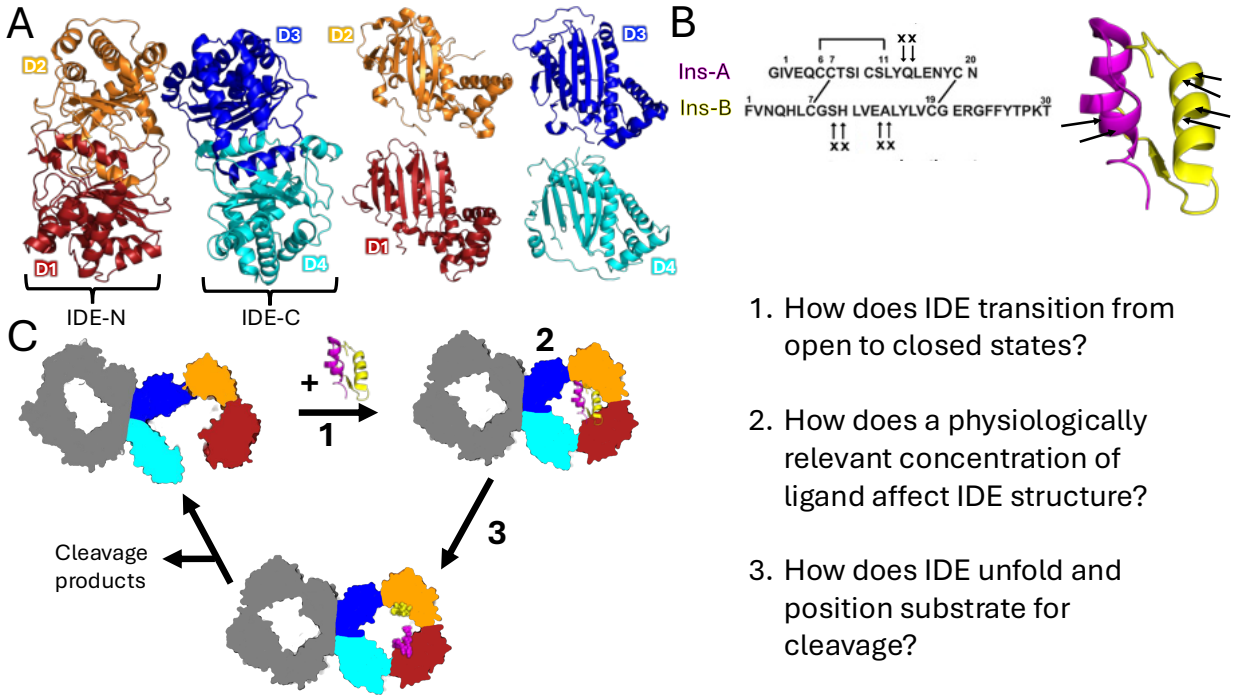

785

786 **Figure 1: Overview of structure and function of IDE.** (A) Overall structure of IDE. IDE is comprised of
787 four structurally homologous domains: D1 (red, residues 43-285), D2 (orange, residues 286-515), D3 (blue,
788 residues 545-768), and D4 (cyan, residues 769-1,016). The domains are arranged in two roughly
789 hemispherical regions that enclose the catalytic chamber referred to as IDE-N (comprised of the D1 and
790 D2 domains) and IDE-C (comprising the D3 and D4 domains), which are joined by a linker region (residues
791 516-544). (B) Primary sequence and overall structure of insulin. Insulin cleavage by IDE as revealed by
792 mass spectrometry (Manolopoulou *et al.*, 2009). Cleavage sites are marked in arrows, which occur within
793 α-helical regions and requires the peptide to be unfolded prior to cleavage. (C) Overview of the IDE catalytic
794 cycle with key questions addressed in this study.

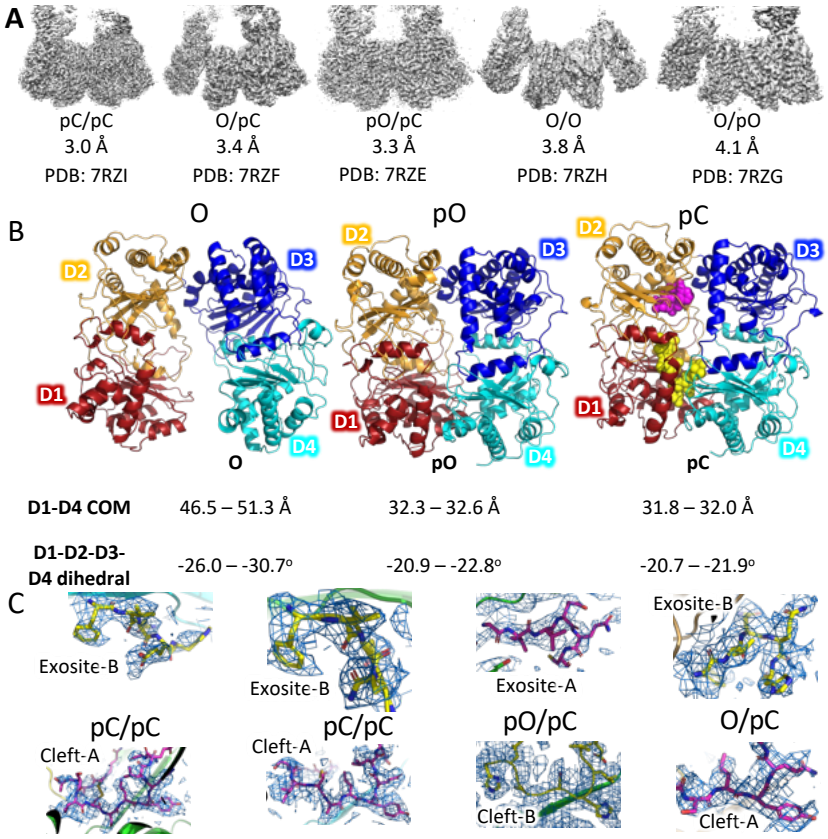

Figure 2: Cryo-EM structures. (A) Overview of the cryo-EM structures. See figure S1 for processing details. **(B)** Comparison of the open (O), partial open (pO), and partial closed (pC) subunit states present in our cryo-EM structures with domain organization. The distance between the D1 and D4 domain centers-of-mass (D1-D4 COM) along with the dihedral angle formed by the D1-D2-D3-D4 domain centers-of-mass (D1-D2-D3-D4 dihedral) described in Zhang et al. (21) and depicted in Figure 3 – figure supplement 1 were used as biologically important criteria to quantify observed conformations. **(C)** Insulin density and corresponding model in our cryo-EM structures. Both the A chain (magenta) and B chain (yellow) can fit the density in the exosite and catalytic cleft.

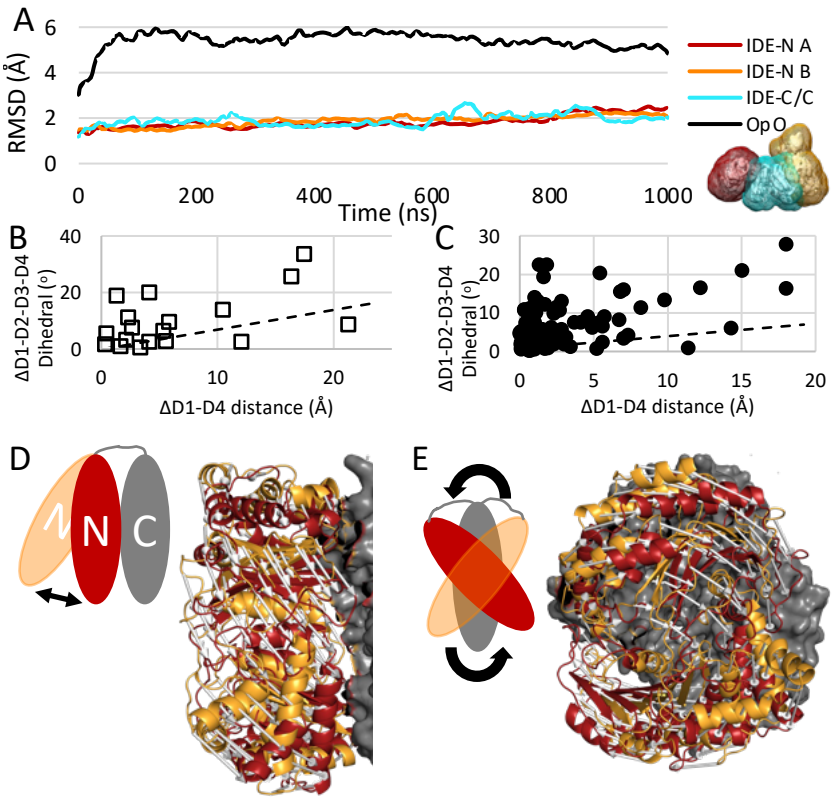

Figure 3: Conformational dynamics of IDE implied by structural heterogeneity. (A) All-atom MD simulations analysis. The primary source of structural variance (RMSD) results from the IDE-N moving against IDE-C as a rigid body. Rigid bodies were defined as colored for multibody refinement in RELION. **(B-C)** Multibody analysis. The range of conformational variance described by the top principal component vectors displays an unexpectedly high degree of rotational motion, as measured by the change in D1-D2-D3-D4 dihedral angle across each vector's gradient of structural heterogeneity, in both the absence **(B)** and presence **(C)** of insulin compared to the expected open-close transition pathway predicted from a linear interpolation of the experimentally determined structures of IDE (dashed line, Figure 3 – figure supplement 1). Two dominant components of structural variance are revealed from multibody analysis: **(D)** where IDE-N swings relative to IDE-N about the inter-domain linker, and **(E)** where IDE-N rotates against IDE-C. Starting (orange) and ending (red) states of IDE-N shown with pathway depicted by arrows. IDE-C shown as gray surface.

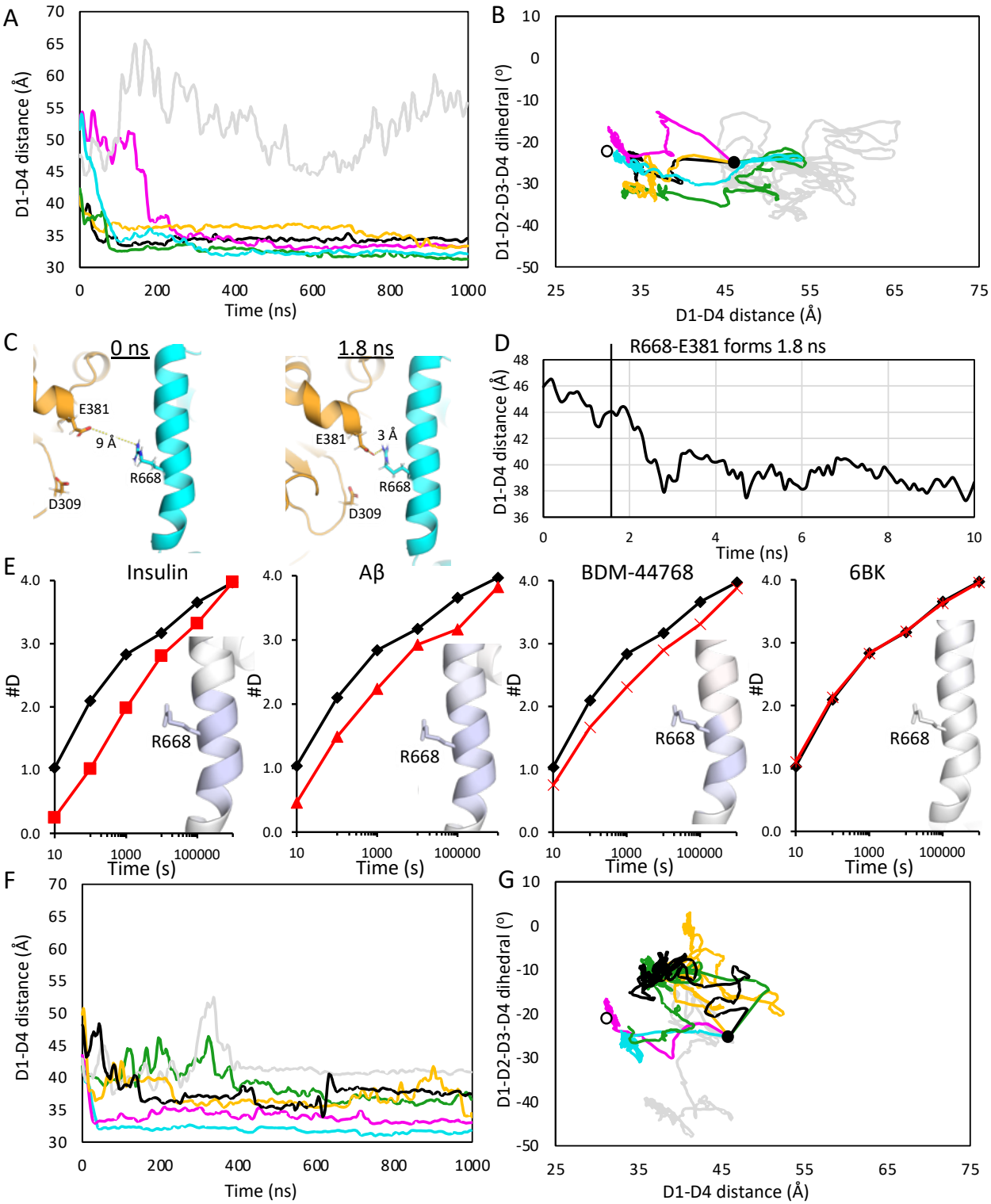

Figure 4: All-atom MD reveals a molecular basis for IDE conformational dynamics. **(A)** Measurements of the O subunit D1-D4 distance over the course of six separate microsecond long all-atom MD simulations of WT IDE. Of which, the open subunit closed in 5 of the 6 simulations. **(B)** Plot of the O subunit D1-D4 distance vs the D1-D2-D3-D4 COM dihedral angle over the course of the simulation of WT IDE. The open

822 subunits displayed a variety of closing pathways and did not close to a consensus structure. Starting
823 structure shown as black dot, pO structure shown as white dot. **(C)** R668 acts as a guidepost residue,
824 rapidly interacting with D309 or E381. Formation of this interaction is associated with rapid closing, as
825 measured by a decrease in D1-D4 distance **(D). (E)** Hydrogen-deuterium exchange mass spectrometry
826 highlights the importance of R668 in mediating the open-close transition. In the presence of insulin (panel
827 1, red), Aβ (panel 2, red) , and BDM-44768 (panel 3, red), all of which promote IDE closing, the peptide
828 containing R668 shows reduced deuterium exchange relative to apo-IDE (black), yet in the presence of 6bk
829 (panel 4, red), which does not promote closing, there is no difference in the exchange rates for the R668
830 containing peptide relative to apo-IDE (black). Helix containing R668 colored by red (increase) – white (no
831 change) – blue (decrease) gradient depicting the degree of deuterium exchange relative to apo-IDE. **(F)**
832 Measurements of the O subunit D1-D4 distance over the course of six separate microsecond long all-atom
833 MD simulations of IDE R668A. **(G)** Plot of the O subunit D1-D4 distance vs the D1-D2-D3-D4 COM dihedral
834 angle over the course of the simulation of IDE R668A. The six separate microsecond long simulations
835 indicate that an R668A mutation significantly alters the closing dynamics of IDE **(F)** and increases the
836 rotational motion **(G)** relative to WT (panels **A** and **B** respectively). Starting structure shown as black dot,
837 pO structure shown as white dot.

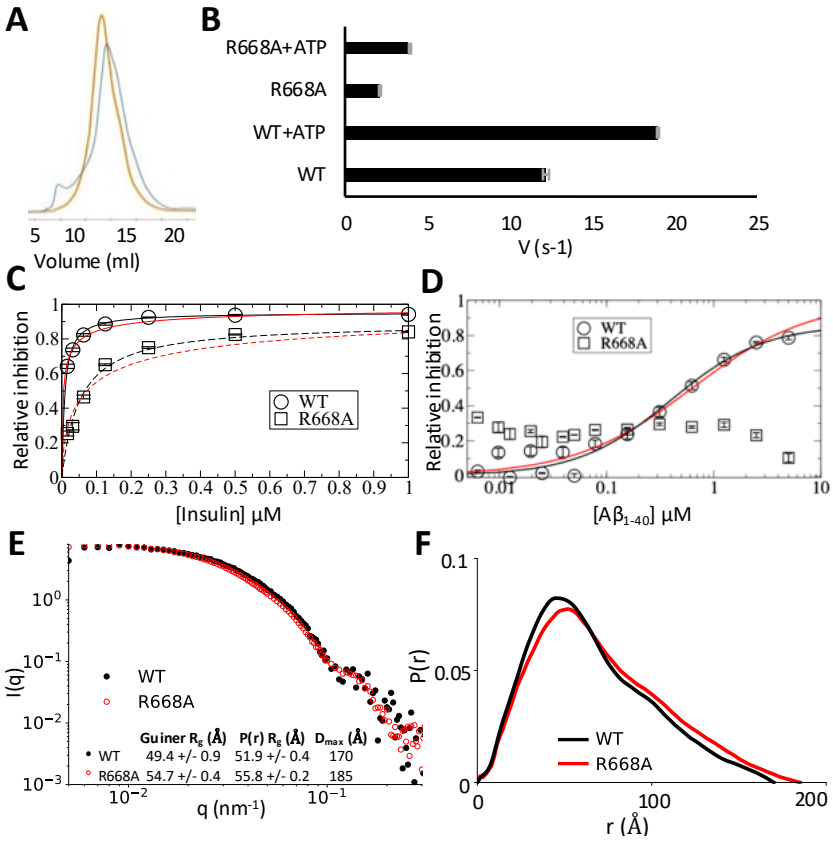

838

839 **Figure 5: R668A alters IDE activity *in vitro* (A)** Elution profile of WT IDE (blue) compared to the R668A
840 mutant (orange) from a S200 SEC column. (**B**) Degradation of the fluorescent substrate MCA-
841 RPPGFSAFK(Dnp) by WT IDE and the R668A construct in the presence and absence of ATP. Data

842 represents the average initial velocities of three replicates performed at a protein concentration of 3.125
843 nM. Error bars (gray) represent the standard error. **(C)** Inhibition of MCA-RPPGFSAFK(Dnp) degradation
844 by WT IDE (circles, solid fit lines) and IDE R668A (squares, dashed fit lines) in the presence of varying
845 amounts of insulin. Data was fit to the Michaelis-Menten (black) and Hill equations (red). Relevant
846 parameters, Michaelis-Menten: WT: χ^2=0.001, V_{max}=0.951, K_i=8.3 nM; R668A: χ^2=0.005, V_{max}=0.892, K_i=52
847 nM; Hill: WT: χ^2=0.009, n=0.55, K_i=51 nM; R668A: χ^2=0.055, n=0.61, K_i=198 nM. Error bars represent
848 standard error, data points represent the average of three replicates. **(D)** Inhibition of MCA-
849 RPPGFSAFK(Dnp) degradation by WT IDE (circles, solid fit lines) and IDE R668A (squares, dashed fit
850 lines) in the presence of varying amounts of insulin. WT data was fit to the Michaelis-Menten (black) and
851 Hill equations (red), R668A data could not be fit to either equation, indicating that the mutation confers
852 substrate-specific altered enzyme kinetics. Relevant WT parameters, Michaelis-Menten: χ^2=0.066,
853 V_{max}=0.823, K_i=353 nM; Hill: χ^2=0.08, n=0.72, K_i=688 nM. **(E)** SEC-SAXS profile of WT (black) and R668A
854 (red) constructs with Rg values calculated by both the Guinier and Porod methods along with Dmax derived
855 from the P(r) function **(F)**.

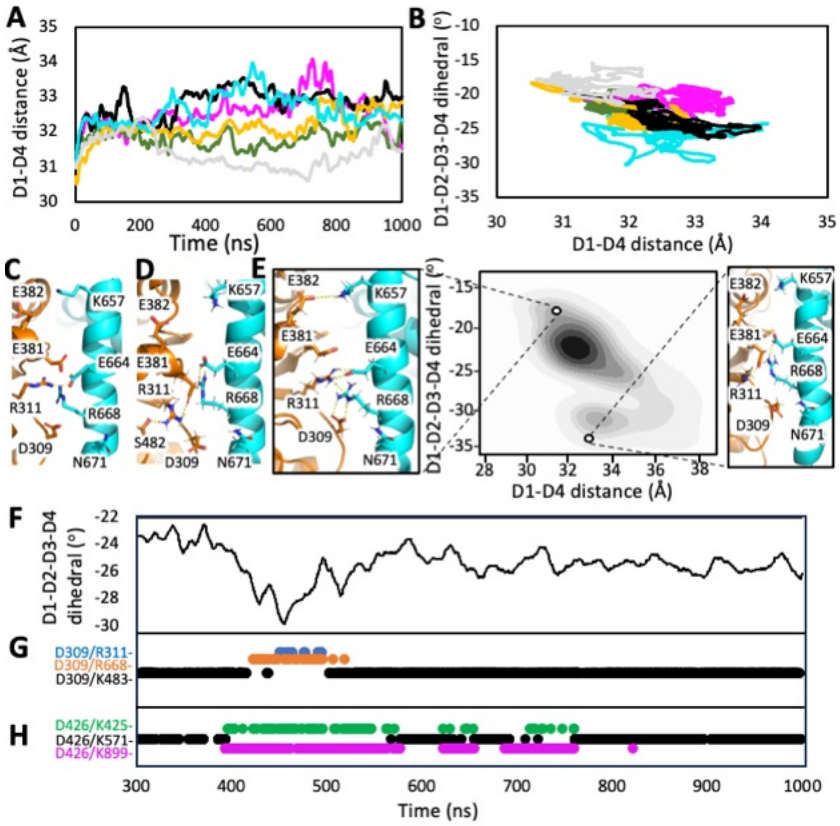

856

857 **Figure 6 Structural basis of closed state conformational dynamics. (A)** Measurements of the pO
858 subunit D1-D4 distance over the course of six separate microsecond long all-atom MD simulations of WT
859 IDE. **(B)** Plot of the pO D1-D4 distance vs the D1-D2-D3-D4 COM dihedral angle over the course of the
860 simulation of WT IDE. **(C)** IDE-N/C interface previously solved crystal structures (PDB:2G47 shown) shows
861 side chains are ill-positioned for interaction. **(D)** IDE-N/C interface formed upon open subunit closing in our

862 MD simulations reveals a complex hydrogen bonding network. **(E)** Heat map showing conformational
863 geometries that were preferentially sampled in our MD simulations by the open subunits upon closing.
864 Insets highlight how the IDE-N/C interface changes to permit interdomain motion. **(F)** Plot of the O subunit
865 D1-D2-D3-D4 dihedral angle during a subset of a single WT IDE MD simulation after the open-close
866 transition has been completed. Charge-swapping between residues at the IDE-N/C interface is associated
867 with changes in the D1-D2-D3-D4 dihedral. **(G)** For most of the simulation, D309 interacts with K483 (black),
868 however, this interaction is broken for ~100 ns, during which D309 instead interacts with R311 (blue) and
869 R668 (orange). **(H)** For most of the simulation, D426 interacts with K571 (black), yet this interaction is
870 periodically broken, and D426 instead interacts with K425 (green) and K899 (magenta). When these events
871 of charge-swapping coincide with D309 charge-swapping **(G)**, they are associated with a large change in
872 the D1-D2-D3-D4 dihedral angle **(F)**. When they occur alone, the effect on D1-D2-D3-D4 dihedral is smaller.

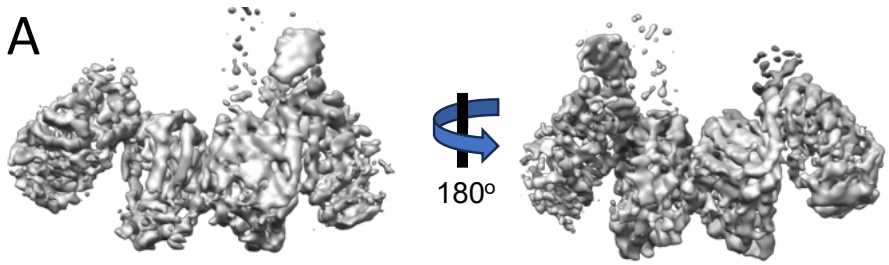

B

	Chain A	Chain B
D1-D4 COM	46.8 Å	55.1 Å
D1-D2-D3-D4 dihedral	-30.4°	-36.5°

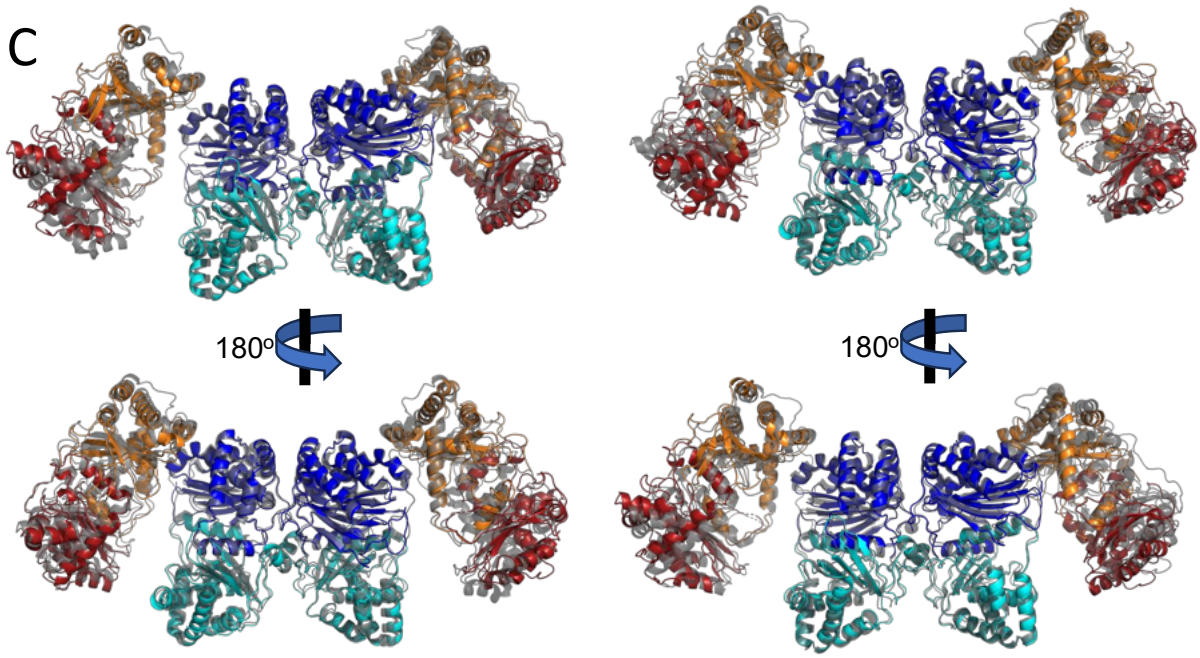

9Y0H vs 7RZH

9Y0H vs 6B7Y

D

Conformational distribution of IDE by condition

Apo-IDE	IDE+Insulin (2:1)	IDE+Insulin (1:5) long	IDE+Insulin (1:5) short
	63% pC/pC		
72.8% O/pO	15.5% O/pO		
16% O/O	14.3% O/pC	100% pC/pC	100% O/O
11.2% pO/pO	3.6% O/O		
	3.6% pO/pC		

Figure 7: Time-resolved cryo-EM of IDE+insulin reveals a new O/O state. (A) 5.1 Å reconstruction of IDE+Fab rapidly mixed with a 5x molar excess of insulin and vitrified with a mix-to-freeze time of 123 milliseconds. **(B)** Measurements (as in Fig. 2) of the distance between the D1-D4 centers-of-mass and dihedral angle formed by the D1-D2-D3-D4 centers-of-mass as indicators of the “openness” of the structure

878 depicted in (A). **(C)** Alignment of the O/O state from our rapid-mixing dataset (domains colored as in Fig. 1)
879 compared to the previously solved O/O states (gray, as labeled). **(D)** Overview of the conformational states
880 adopted by IDE in all 4 available cryo-EM datasets with corresponding percentage of particles mapping to
881 each state (Zhang *et al.*, 2018)(this work).

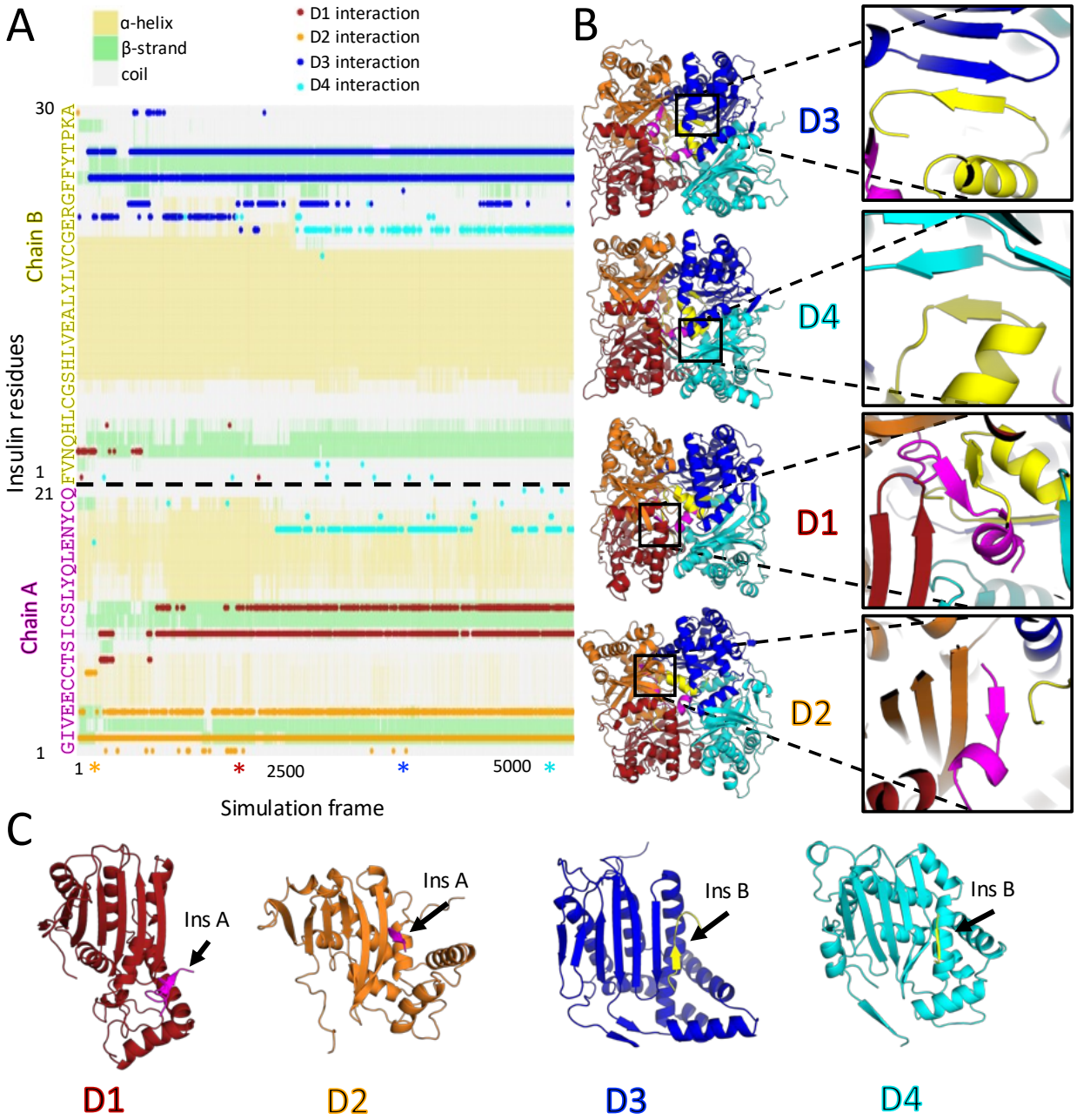

882

883 **Figure 8: Upside analysis of IDE-insulin interactions. (A)** Transient cross-β-strand interactions between
884 insulin and IDE. Secondary structure (gray: coil, green: β-strand, yellow: α-helix) for each insulin residue
885 (Y-axis) over the course (X-axis) of a representative Upside simulation. Points indicate predicted hydrogen
886 bond interactions between IDE and insulin, colored by which domain of IDE that insulin residue is interacting
887 with (D1: red, D2: orange, D3: blue, D4: cyan). Stars below the X-axis indicate frames from which structures
888 were extracted for panel B. **(B)** Structure of IDE/insulin complex in Upside simulations at frames indicated
889 in (A). IDE domains colored as in (A), insulin shown in magenta (chain A) and yellow (chain B). Inset
890 highlights the intermolecular cross-β sheets formed between IDE and insulin within each of the four
891 homologous IDE domains. **(C)** Individual domains of IDE, colored as in (A), extracted from (B) and oriented
892 to demonstrate the structural conservation of intermolecular cross-β-sheet formation with bound insulin
893 (colored as in B).

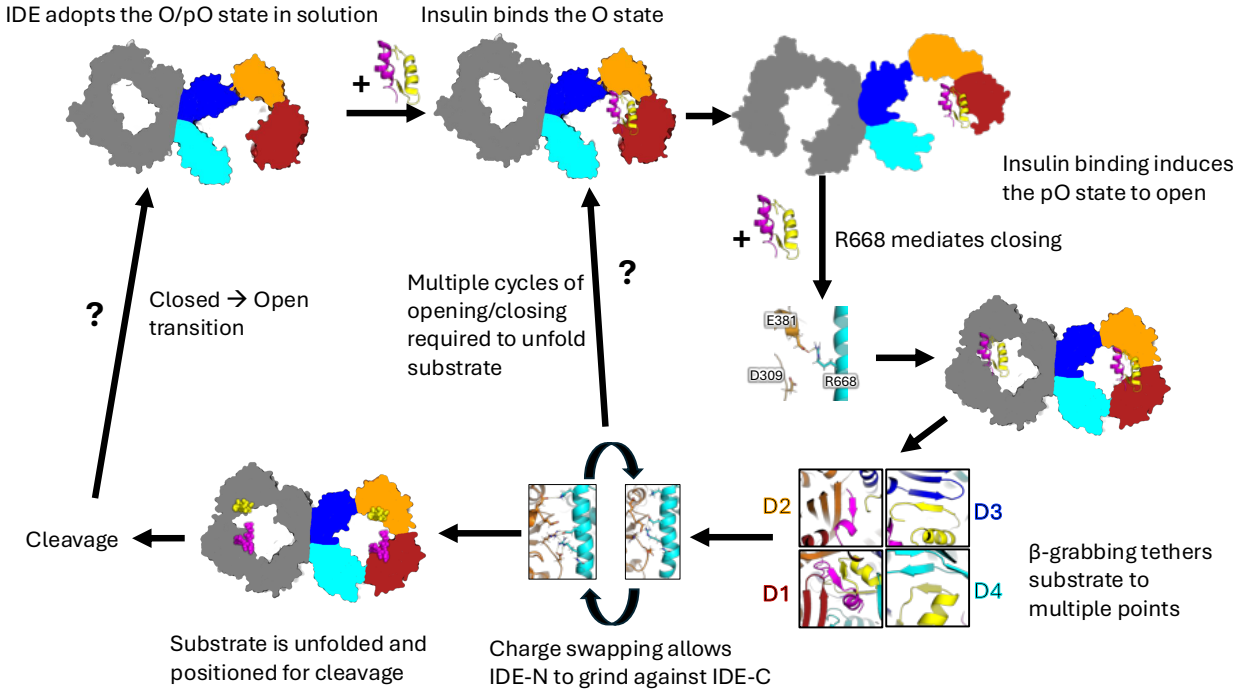

894

895 **Figure 9: Model for the catalytic cycle of IDE**. The details are described in discussion. For simplicity,
896 only the scenario involving the addition of a second insulin molecule is illustrated, although this is not
897 required for the catalytic cycle. The mechanism by which IDE transitions between closed and open states
898 remains unknown and is therefore indicated with question marks.

899 **Supplements**